

Highlights

Energy and Flow Effects of Optimal Automated Driving in Mixed Traffic: Vehicle-in-the-Loop Experimental Results

Tyler Ard, Longxiang Guo, Robert Austin Dollar, Alireza Fayazi, Nathan Goulet, Yunyi Jia, Beshah Ayalew, Ardan Vahidi

- Mixes physical vehicles with virtual traffic environments for energy and flow evaluation from integrated vehicle control algorithms.
- Measures conventional and electric powertrain types for energy effects.
- Introduces probabilistic constraints to balance safety and traffic flow considerations.
- Combines data-driven techniques with classical techniques for automated vehicle actuation.

Energy and Flow Effects of Optimal Automated Driving in Mixed Traffic: Vehicle-in-the-Loop Experimental Results

Tyler Ard^a, Longxiang Guo^b, Robert Austin Dollar^a, Alireza Fayazi^a, Nathan Goulet^b, Yunyi Jia^b, Beshah Ayalew^b and Ardalan Vahidi^{a,*}

^aDepartment of Mechanical Engineering, Clemson University, Clemson, SC

^bDepartment of Automotive Engineering, Clemson University, Greenville, SC

ARTICLE INFO

Keywords:

vehicle-in-the-loop
virtual traffic microsimulation
probabilistic constraints
energy efficiency
model predictive control
data-driven control

ABSTRACT

This paper experimentally demonstrates the effectiveness of an anticipative car-following algorithm in reducing energy use of gasoline engine and electric Connected and Automated Vehicles (CAV), without sacrificing safety and traffic flow. We propose a Vehicle-in-the-Loop (VIL) testing environment in which experimental CAVs driven on a track interact with surrounding virtual traffic in real-time. We explore the energy savings when following city and highway drive cycles, as well as in emergent highway traffic created from microsimulations. Model predictive control handles high level velocity planning and benefits from communicated intentions of a preceding CAV or estimated probable motion of a preceding human driven vehicle. A combination of classical feedback control and data-driven nonlinear feedforward control of pedals achieve acceleration tracking at the low level. The controllers are implemented in ROS and energy is measured via calibrated OBD-II readings. We report up to 30% improved energy economy compared to realistically calibrated human driver car-following without sacrificing following headway.

1. Introduction

Modern camera-based automated vehicles were popularized by efforts such as (Pomerleau, 1990) or (Thrun et al., 2006), conceptually demonstrating that challenges of vehicle localization and control in off-road and low-traffic environments could be overcome. Since then, community perspective has become commercially motivated to automate vehicle control on roadways mixed with human-driven traffic. Promising advances in automation could realize unprecedented improvements in network flow efficiency, energy utilization, and safety by leveraging data as available from traffic infrastructure and other drivers (Vahidi and Sciarretta, 2018).

Traffic throughput issues have been experimentally shown in commercially produced adaptive cruise controllers, in which they can be string unstable - causing disturbance propagation to traffic upstream and reducing overall network efficiency (Gunter et al., 2019). However, experiments in automated vehicles have shown string stabilizing effects by leveraging vehicle-to-vehicle connectivity. (Ploeg et al., 2011) give a classically-based connected and adaptive cruise controller for improving string stability, whereas (Hajdu et al., 2020) additionally account for uncertainty in human driving to show robust string stabilizing cruise control. More specifically, improved traffic throughput has been quantified during simulation of highway scenarios with partially mixed strings of automated vehicles. Such topics have actuated vehicle motion using reactive car-following controllers (Talebpoor and Mahmassani, 2016; Liu et al., 2020), and could additionally utilize centralized prioritization schemes when in highway merging zones (Rios-Torres and Malikopoulos, 2017, 2018).

We focus on additionally quantifying improved energy efficiency in automated driving from flow experiments via anticipative car-following. Motion planning is done by casting an optimal control problem (OCP) through model predictive control (MPC). Such approaches form a look-ahead control scheme, and as such can utilize preview through connectivity or prediction to better plan vehicle maneuvers - similar to those presented in (Zheng et al., 2017) for traffic smoothing. Energy-motivated nonlinear approaches such as (Turri et al., 2017) are experimentally shown to improve energy economy by up to 50% over the baseline control for a high-disturbance scenario when utilizing connected preview, whereas linearizations of similar OCPs would not rely on nonlinear program solvers while still showing notable energy improvements (Ard et al., 2020). Further experiments utilizing hardware-in-the-loop setups have quantified

*Corresponding author

trard@clemson.edu (T. Ard); avahidi@clemson.edu (A. Vahidi)

ORCID(s): 0000-0001-9816-7578 (T. Ard); 0000-0002-1669-3345 (A. Vahidi)

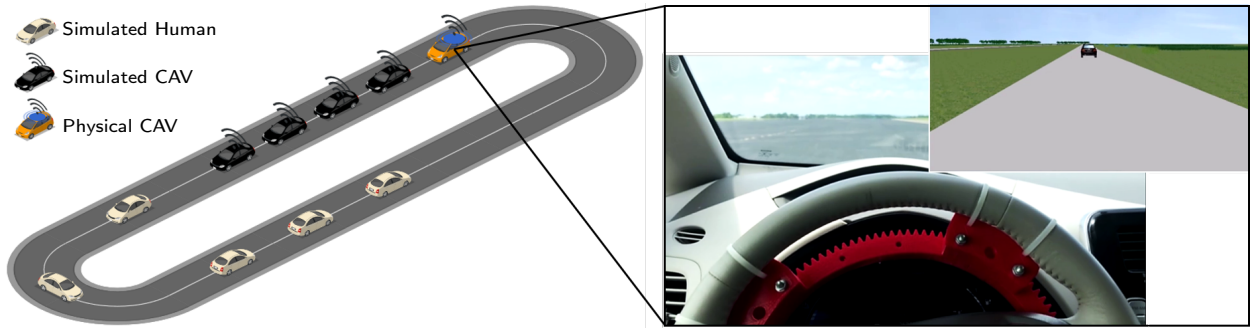


Figure 1: Visualization of the Vehicle-in-the-Loop environment from the real vehicle perspective in both simulation and reality. The physical vehicle is embedded into a virtual environment and interacts with virtual drivers. The diagram on the left was generated at icograms.com

fuel and emission reductions from a combustion vehicle (Schmied et al., 2015) using preview-based control. Specifically addressing energy economy and traffic compactness, (Kamal et al., 2011) introduce a multi-objective approach that minimizes error from desired time gap behind the preceding vehicle and vehicle acceleration. This work employs the MPC approach proposed in (Dollar and Vahidi, 2018; Ard et al., 2019).

When connected preview is not available, challenges of safety can arise due to improper anticipation of the behavior of other vehicles, as well as sensing and recognition error of obstacles on the road (NTSB Media Relations, 2020). To address issues of safety during motion planning, barrier methods (Schmied et al., 2015) or invariant set constraints (Gao et al., 2014) can be introduced with MPC for control robustness. To further support the multi-objective of promoting both traffic compactness and energy economy, we instead introduce a probabilistic approach, similar to that of (Zhang and Vahidi, 2011), for robustness by quantifying uncertainty in prediction of the preceding vehicle (Ard et al., 2019).

Ring experiments such as (Stern et al., 2018) leverage a small string of vehicles to create macroscopic traffic effects from vehicles interacting with each other because no vehicle is in free flow. As a complement to experiments of this nature, a Vehicle-in-the-Loop (VIL) approach is presented here to additionally co-simulate virtual drivers and create a larger string of vehicles for more realistic traffic scenarios. This is conducted in a safe virtual reality mixed with a traffic microsimulation (Ard et al., 2019; Fayazi et al., 2019; Liu et al., 2020), and has potentially additional applications for studying urban environments with intersection control, highway and merging scenarios, parking maneuvers, etc.

We report on experimental details and analysis of the implementation of anticipative car-following algorithms proposed in (Dollar and Vahidi, 2018; Ard et al., 2019). Figure 1 demonstrates the virtual reality viewpoint of the VIL environment, where the physical vehicle is embedded in simulation. This work is focused on the impact of connectivity for predicting traffic events and improving subsequent motion planning - with an emphasis on increasing energy efficiency.

The contributions of this paper are the following:

1. A VIL framework is proposed for real time co-simulation of cyber-physical systems of traffic simulation environments and physical automated vehicles.
2. An anticipative and connected vehicle guided with MPC is experimentally studied for traffic flow and energy benefits. Safety and compactness robustification is handled through the use of probabilistic constraints in the absence of connectivity: explicitly considering the uncertainty in predicted position of the preceding vehicle.
3. Instrumentation of combustion engine and electric vehicles is shown through pedal and steering actuators, and vehicle localization is handled through positioning and inertial measurements. Nonlinearities in pedal-to-engine transitions are approximated through data-driven maps for command of vehicle acceleration.
4. Quantitative analysis is done to verify measured energy improvements of the automated control scheme for both a combustion engine and an electric vehicle in several traffic environments. Additionally, traffic flow impacts of the control scheme are shown.

The remainder of this paper is organized as follows. Section 2 describes the VIL architecture and how major system components relate to each other - motivating later discussion. Section 3 then describes the MPC designed for high-level longitudinal control, and presents both the connected and unconnected variants of the controller. Baseline high-level control modeled to capture human drivers are given in Section 4. The vehicle instrumentation and low-level control design are presented in Section 5. To study energy for both combustion engine and electric vehicles, Section 6 presents the modeling techniques used to analyze on-board diagnostics (OBD) signals as collected during experiments. Then, experimental scenario descriptions are given in Section 7. Finally, Section 8 discusses the results for the experiments, and Section 9 concludes the work as presented here.

2. Vehicle-in-the-Loop simulator setup

Vehicle-in-the-Loop is an automated driving virtual simulation in which a physical vehicle (ego) is embedded into a traffic scenario with the goal of evaluating performance of such cyber-physical systems in a realistic manner without compromising safety. VIL is used here to evaluate energy performance of both a Mazda CX-7 combustion engine vehicle and a Nissan Leaf electric vehicle.

VIL is developed in three component layers:

1. the server layer, responsible for conducting remote simulation of a traffic environment and communicating simulation status to the ego vehicle at fixed time intervals,
2. the autonomous client layer, responsible for control decisions for the ego vehicle at a high-level trajectory planning and a low-level execution, as well as vehicle localization in the traffic environment and communication of vehicle status at fixed intervals in time, and
3. the vehicle hardware layer, which features pedal and steering actuators fit to command the vehicle autonomously, as well as an OBD-II port which publishes select signals from the vehicle electronic-control-unit (ECU).

Figure 2 depicts the major nodes and signals of the VIL architecture. Software specifics are detailed for the remainder of this section.

2.1. Simulation-reality synchronization

To restrict both the ego and virtual vehicles to drive on the same road map and allow them to directly interact, a key design is made in how the roads of the simulation network are defined. First, a desired geometry is driven on a test track and positional data from the RTK-GPS servicing the ego vehicle is recorded. Then, the RTK signals are mapped directly to the simulation environment to construct the roadways $(x, y)_{\text{RTK}} \mapsto (x, y)_{\text{Sim}}$. It then follows that the ego vehicle can be embedded in simulation in real-time by communicating its position, velocity, and heading (x, y, v, θ) tuple.

2.2. Simulation data exchange

A client-server architecture was designated between the ego vehicle and simulation computer so that computational load could be split between multiple computers. Such a setup also has the advantage of allowing co-simulation of multiple clients at once - suitable for future experiments.

In this case, exchange of key data between simulation and the ego vehicle was defined using a Google Protocol Buffer (Protobuf) serialization to byte arrays and then broadcast through the User-Datagram Protocol (UDP) socket communication. UDP was chosen because of its low-latency data exchange and is suitable in systems with lower chances of packet loss. Protobuf is a class-based API that allows the user to define the data structures to be included in a message, then handles packing and unpacking the messages when sending or receiving (Google Inc., 2020).

Appendix A details the structure of the Protobuf message used. The data exchanged between the physical vehicle and the simulation server lies in four categories: 1) Subscription/Unsubscription Message: A physical vehicle subscribes to the simulation server at the beginning of VIL simulations, or unsubscribes to end the simulation, 2) V2Sim Message: A physical vehicle transmits its updates (x, y, v, θ) to the simulation server, 3) Sim2V Message: the simulation server transmits information of the simulated vehicles surrounding the physical vehicle, and 4) V2V Message: the simulated and physical vehicles exchange planned trajectories for connected vehicle guidance (MPC-C). The simulation server was connected to the vehicle-control computer via ethernet, and V2V communication delay in MPC-C

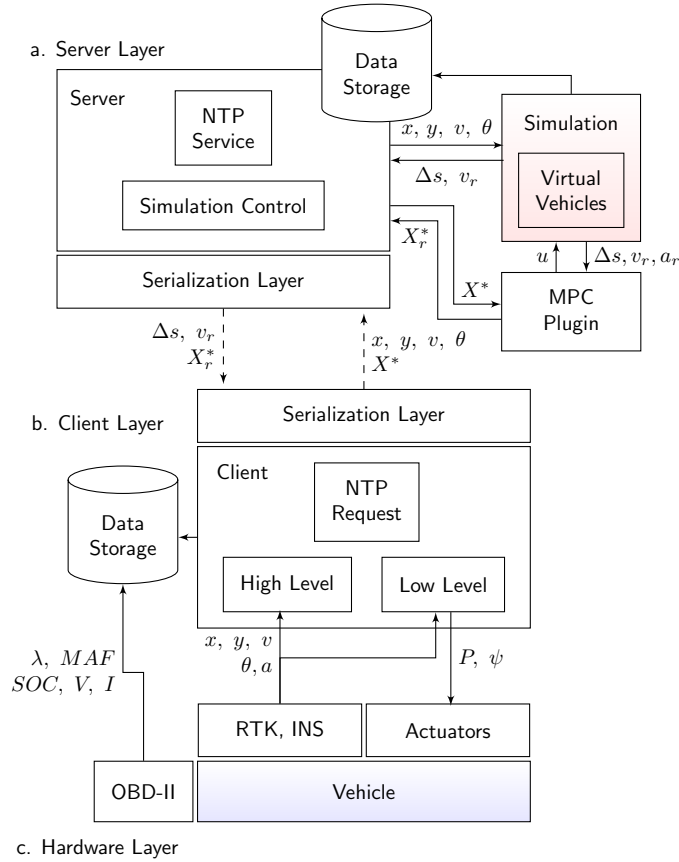


Figure 2: Local network of the VIL software and hardware

messages was emulated by delaying their transmission by 100 ms. This was done to account for typical latencies of cellular or DSRC communication technologies that would be used in V2V experiments - as opposed to the VIL approach espoused here.

When conducting experimental microsimulations - using commercial software PTV VISSIM - a plugin was created to define automated vehicle behavior using model predictive control (Ard et al., 2019). A shared memory interface was then established to handle interprocess communication between the server process and the plugin - so that communication between physical and virtual CAVs could occur. By this, the state preview generated from the MPC preceding vehicle, X_r^* , is extracted and communicated to the ego, and the ego shares its state preview, X^* , with simulation.

2.3. Simulation and control timing

Timing mechanisms are defined in the server layer for precisely controlling the simulation environment to run in real-time and broadcast updates on its status in regular intervals of 10 hz, and are defined in the client layer for broadcasting the ego vehicle's status in regular intervals of 10 hz - so that the vehicle can provide feedback to the simulation for surrounding virtual traffic to react to. Because multiple computers are involved, a Network Time Protocol (NTP) was introduced to synchronize the clocks and regularly measure communication delay (Mills, 2010). In this case, the client polls the server for its clock time, and makes an adjustment to its own clock by measuring a time-offset t' , and round-trip delay Δt ,

$$t' = \frac{(t_1 - t_0) - (t_3 - t_2)}{2} \quad (1a)$$

$$\Delta t = (t_3 - t_0) - (t_2 - t_1) \quad (1b)$$

where t_0 , t_3 are the client's request and reception message timestamps, and t_1 , t_2 are the server's reception and response message timestamps. Most recent round-trip delays are used by the client and server to interpolate positional data from the ego vehicle and its preceding vehicle using their respective current velocity $s^+ = s + v\Delta t/2$.

Further design elements of the VIL architecture are described in the following sections.

3. Chance-constrained MPC for car-following

The proposed energy-efficient CAV controller uses model predictive control based on (Dollar and Vahidi, 2018; Ard et al., 2019) to consider preview information when computing the ego vehicle's control move. It requires a longitudinal vehicle dynamics model that predicts how the ego vehicle will respond to a given sequence of control inputs over a finite time called the prediction horizon. Armed with such a model, the controller solves a mathematical program to minimize an objective subject to constraints. Since the preceding vehicle (PV) may be either connected or not, different algorithm variants are used to handle the connected (MPC-C) and unconnected (MPC-U) cases. The unconnected case involves particularly significant uncertainty that chance constraints help to manage.

This section will first introduce the model before developing the optimal control problem (OCP). Then, the connected and unconnected variants are described including the chance constraint formulation in the latter case.

3.1. Control modeling

Since the optimal control problem is solved numerically, computation time is an important consideration in MPC design. Problems using linear models, quadratic objectives, and affine constraints become quadratic programs (QPs), which can be solved quickly online¹. Hence, the following linear double-integrator with low-pass filter is chosen to approximate the vehicle dynamics.

$$\frac{d}{dt} \begin{bmatrix} s \\ v \\ a \end{bmatrix} = \begin{bmatrix} 0 & 1 & 0 \\ 0 & 0 & 1 \\ 0 & 0 & -\tau_a^{-1} \end{bmatrix} \begin{bmatrix} s \\ v \\ a \end{bmatrix} + \begin{bmatrix} 0 \\ 0 \\ \tau_a^{-1} \end{bmatrix} u \quad (2)$$

In Eqn. (2), the position s , velocity v , and actual acceleration a form the state vector. The acceleration state lags the commanded acceleration u with time constant τ_a . In this experimental study, $\tau_a = 0.275$ s is used to approximate the lumped response of the acceleration controller, actuator, and vehicle powertrain or brake system.

3.2. Optimal control problem

The optimal control problem (OCP) should fulfill several purposes: improving the ego vehicle's energy efficiency, smoothing the overall traffic stream, maintaining road throughput, guaranteeing safe and feasible operation, and limiting computation time. In the proposed formulation, a weighted objective minimizes the squares of acceleration and headway tracking error, which can both be expressed as quadratic functions of state variables. Such an objective reduces unneeded braking, and reduces electric resistance losses in electric vehicles (EVs). While higher acceleration can sometimes improve efficiency in internal combustion engine vehicles (ICEVs) (Han et al., 2019), in some applications minimizing acceleration helps to avoid inefficient high-power enrichment as demonstrated in Section 8.

The following OCP yields the vector U of control variables u at each stage i in the N -step prediction horizon and utilizes additional decision variables ϵ to soften pure state constraints

$$\min_{U, \epsilon} \quad q_g (s(N) - s_t(N))^2 + q_a a^2(N) + \sum_{i=0}^{N-1} \left[q_g (s(i) - s_t(i))^2 + q_a (u^2(i) + a^2(i)) \right] + \sum_{j=1}^4 \rho_j \epsilon_j \quad (3a)$$

$$\text{s.t.} \quad 0 - \epsilon_3 \leq v(i) \leq \bar{v}(i) + \epsilon_2 \quad (3b)$$

$$\underline{u} \leq u(i) \leq \min \{ m_1 v(i) + b_1, m_2 v(i) + b_2 \} \quad (3c)$$

$$a(i) \leq \min \{ m_1 v(i) + b_1, m_2 v(i) + b_2 \} + \epsilon_4 \quad (3d)$$

$$s(i) \leq s_a(i) - \underline{d} + \epsilon_1 \quad (3e)$$

where $s_t(i) \triangleq s_r(i) - Tv(i) - d_r$, T is the target time headway, s_r is the preceding vehicle's (PV's) position, and d_r is the minimum target distance. Combining U with the ego's current state and linear model yields the ego's future state trajectory. Table 1 defines the MPC parameters and lists their values.

¹These experiments used the Gurobi optimizer (Gurobi Optimization, 2020) to solve the QP - solving in 2 ms on average.

Table 1
MPC parameters for the unconnected (MPC-U) and connected (MPC-C) cases.

Symbol	Description	MPC-U	MPC-C
N	horizon length	16 [s]	17 [s]
q_a	acceleration penalty	2050	4000
q_g	gap penalty	1	1
T	reference headway	1.3 [s]	0.0 [s]
d_r	reference gap	2.0 [m]	6.0 [m]
\underline{d}	minimum gap	2.0 [m]	2.0 [m]
ρ	soft constraint penalty	{1e6, 5e5, 5e5, 1e6}	
m	acceleration constraint slope	{0.285, -0.121}	
b	acceleration constraint intercept	{2.00, 4.83}	
\underline{u}	minimum acceleration constraint	-5.5 [m/s ²]	
τ	acceleration lag	0.275 [s]	
Δt_h	discretization stepsize	1.0 [s]	

Equation (3b) prevents the controller from driving in reverse or exceeding the speed limit \bar{v} and is softened with slack variables ϵ_3 and ϵ_2 , respectively. The vehicle hardware has limited braking capacity \underline{u} and acceleration capacities that Eqns. (3c, 3d) approximate. The slack variable ϵ_4 softens the acceleration state constraints; however, the input constraints are hard. Table 1 provides the acceleration constraint coefficients m and b . Collision avoidance is accomplished using Eqn. (3e), where s_α denotes the position ahead of which the PV will lie with probability α and \underline{d} is the minimum safe distance. The collision avoidance constraint is softened with slack ϵ_1 to guarantee feasibility even under unexpectedly harsh PV braking. The rest of this section will discuss how s_α is obtained in MPC-C and MPC-U.

3.3. Connected case (MPC-C)

When a predictive CAV leads the ego vehicle in the string, the PV's planned trajectory is available through connectivity for all stages i . In this case, s_r and s_α are both equal to the planned positions of the PV. This trajectory is accurate enough that no probabilistic safety margin is needed.

3.4. Unconnected case (MPC-U)

If a CAV follows a conventional vehicle that does not communicate its future plans, that CAV must predict s_r and s_α . To obtain the nominal PV position s_r , prediction assumes a constant acceleration a_r with saturation of the predicted PV speed v_r to its minimum or maximum.

$$a_r(i) = \begin{cases} a_r(0) & 0 < v(i) < \bar{v} \\ 0 & \text{otherwise} \end{cases} \quad (4a)$$

$$v_r(i+1) = \min \{ \max \{ v_r(i) + \Delta t_h a_r(i), 0 \}, \bar{v} \} \quad (4b)$$

$$s_r(i+1) = s_r(i) + v_r(i) \Delta t_h + \frac{1}{2} a_r(i) \Delta t_h^2 \quad (4c)$$

In reality, the PV's acceleration can change significantly over the prediction horizon. This mismatch between preview and reality can cause collisions if not addressed. A worst-case constraint was used in (Dollar and Vahidi, 2018) to prevent collisions, but the resulting conservatism led to reduced traffic flow in the presence of unconnected vehicles. To improve throughput, (Ard et al., 2019) replaced the worst-case constraint with a less-conservative chance constraint.

In the less-certain unconnected case, $s_\alpha(i)$ in Eqn. (3e) approximates the position that the PV will have reached by prediction step i with probability α . Therefore, the resulting open-loop ego vehicle trajectory avoids the realized PV trajectory at stage i with probability α . The chance constraints consider a stochastic PV state vector $Z_r = [S_r \ V_r \ A_r]^T$. The uncertainty at the current time comes from the acceleration, whose deviation from a_r is assumed normally distributed i.e. $\tilde{A}_r \sim \mathcal{N}(0, \sigma_A^2)$. Thus

$$Z_r(0) = [s_r \ v_r \ a_r]^T + [0 \ 0 \ \tilde{A}_r]^T. \quad (5)$$

This initial distribution is used in (Ard et al., 2019) to derive the future random PV position variable $S_r(i) = s_r + \tilde{S}_r(i)$, where $\tilde{S}_r(i) \sim \mathcal{N}(0, \Lambda_{11}(i))$ with the covariance of the PV's future state as

$$\Lambda(i) = A^i \begin{bmatrix} 0 & 0 & 0 \\ 0 & 0 & 0 \\ 0 & 0 & \sigma_A^2 \end{bmatrix} (A^i)^T, \quad (6)$$

which is obtained by propagating a Gaussian signal through the linear state-space model in Eqn. (2). The probability α can then be expressed in terms of the cumulative distribution function $F_{\tilde{S}_r}(s_\alpha - s_r)$ of \tilde{S}_r , where the argument is the position safety adjustment from the nominal estimate s_r .

$$\alpha = 1 - F_{\tilde{S}_r}(s_\alpha - s_r) \quad (7)$$

Inverting the cumulative density function and exploiting its symmetry yields s_α for a chosen α .

$$s_\alpha(\alpha) = s_r - F_{\tilde{S}_r}^{-1}(\alpha) \quad (8)$$

While (Wan et al., 2017) used a constant value of α , the linear function proposed in (Dollar and Vahidi, 2019) is used here,

$$\alpha(t) = (\underline{\alpha} - \bar{\alpha}) \cdot \frac{t}{t_f} + \bar{\alpha}; \quad t \in [1, 10] \quad (9)$$

where $\underline{\alpha} = 0.5$, $\bar{\alpha} = 0.99999$, and $t_f = 10$ s. Equation (9) thus sets α to a conservative value early in prediction when the controller has little opportunity for closed-loop correction but the variance in PV position is small - and gradually relaxes α later in prediction when the variance in PV position is high but more risk is acceptable. This results in a maximum buffer distance of approximately $s_r - s_\alpha = 9.5$ m when $t = 6$ s.

4. Baseline car-following control

To evaluate the energy and traffic flow impacts of the MPC automated vehicles, both the Wiedemann model (WIE) and Intelligent driver model (IDM) were designated as baseline longitudinal controllers. Both models were tuned to replicate human driving, and have been shown in various literature to well-realize macroscopic traffic effects (Washington State Department of Transportation (WSDOT), 2014; Fellendorf and Vortisch, 2011; Treiber et al., 2000).

Real human drivers were not introduced in this study due to safety concerns of interfacing humans with virtual environments - particularly when driving cars. Human drivers are known to perceive upcoming traffic events by observing behavior of multiple vehicles downstream (Alexander and Lunenfeld, 1986), so realistic human-trial experiments would likely either: 1) involve instrumenting a string of several automated vehicles to drive in front of a test subject - all of which interact with the VIL environment, or 2) introduce a mixed reality headset for the driver to wear. Both cases are interesting and the authors leave them for future studies.

4.1. Wiedemann human driver model

The psycho-physical Wiedemann 74 model, originally published in (Wiedemann, 1974), features distinct modes of: car-following headway tracking, free-driving velocity tracking, emergency braking, and catch-up acceleration. The model additionally limits acceleration capabilities of the vehicle as a function of velocity to model the powertrain. Additionally, by modeling imperfections in human perception of the velocity and acceleration of the preceding vehicle, it features oscillation in the commanded acceleration of the driver at steady tracking.

To build on the model, an updated version was then created specifically for microsimulation software PTV VISSIM - denoted the Wiedemann 99 model (WIE 99). This version expands on the number of parameters available to tune the longitudinal behavior, and because of refined thresholds for the different modes of driving, is preferred for longitudinal modeling (Fellendorf and Vortisch, 2011). The virtual vehicles in VISSIM are controlled by the WIE 99 model and are tuned by the procedure defined in (Ard et al., 2019). Several studies note that the default parameters in VISSIM are sufficient for general simulations, and only careful changes to driver headway are typically needed (Woody, 2006). Here, it was observed that WIE 99 vehicles on average drive with more aggressive headways compared to empirical

Table 2
Wiedemann 99 model parameters

Symbol	Description	Value
CC_0	standstill gap	3.00 [m]
CC_1	desired headway (mean)	1.35 [s]
CC_2	following oscillation amplitude	8.00 [m]
CC_3	distance threshold	-8.00 [m]
CC_4	velocity threshold	-0.35 [m/s]
CC_5	velocity threshold	0.35 [m/s]
CC_6	speed perception threshold	11.4 [1/(m·s)]
CC_7	acceleration oscillation amplitude	0.25 [m/s ²]
CC_8	maximum acceleration (0 km/h)	3.50 [m/s ²]
CC_9	maximum acceleration (80 km/h)	1.50 [m/s ²]
\mathcal{X}	random driver variable in experiments	0.35 [m/s ²]

data. As such, the headways of the VISSIM drivers were adjusted to replicate the data as presented in (Chen et al., 2010).

In addition to using the WIE 99 model for modeling the human drivers in VISSIM, the WIE 99 model was implemented for control of the experimental vehicles as a baseline. The model is reproduced as given in (Vortisch, 2020) and shown in Appendix B. Although VISSIM has since expanded the model and uses additional features and considerations in car-following behavior, it was found that the implementation for the physical cars well-matched VISSIM behavior.

Table 2 gives the parameters for the WIE 99 model used in simulation and in the physical car for experiments.

4.2. Intelligent driver model

The Intelligent driver model (IDM), as originally introduced in (Treiber et al., 2000), is a popular longitudinal controller to model both human behavior and adaptive cruise controllers. For this study, the IDM was tuned to replicate human driving as introduced in (Dollar and Vahidi, 2018) and based on the study by (Pourabdollah et al., 2017). The IDM differs from the WIE model by precisely tracking desired headway in steady conditions and features less aggressive acceleration behavior.

The model computes an acceleration command given instantaneous ego velocity, v , and the differences in the relative position and velocity with respect to the PV, Δs and Δv ,

$$\dot{s} = v \quad (10a)$$

$$\dot{v} = a_0 \left(1 - \left(\frac{v}{v_0} \right)^\delta - \frac{s^*(v, \Delta v)}{\Delta s} \right) \quad (10b)$$

with

$$s^*(v, \Delta v) = s_0 + \max \left\{ 0, T v + \frac{v \Delta v}{2\sqrt{a_0 b_0}} \right\}.$$

Here, a_0 is the maximum acceleration, b_0 is the comfortable deceleration, T is the desired time headway, δ is an acceleration exponent, s_0 is the desired vehicle-to-vehicle gap, and v_0 is the desired velocity.

Table 3 lists the parameters for the IDM used in the experiments.

5. Experimental vehicle adaptations

As mentioned in Section 2, the vehicle required pedal and steering actuators to command the vehicle autonomously. This section introduces the instrumentation of the experimental vehicles and the design and performance of the low-level controllers.

Table 3
Intelligent driver model parameters

Symbol	Description	Value
a_0	maximum acceleration	1.52 [m/s ²]
b_0	comfortable deceleration	3.24 [m/s ²]
T	desired headway	1.02 [s]
s_0	desired standstill distance	10.0 [m]
δ	acceleration exponent	4 [-]

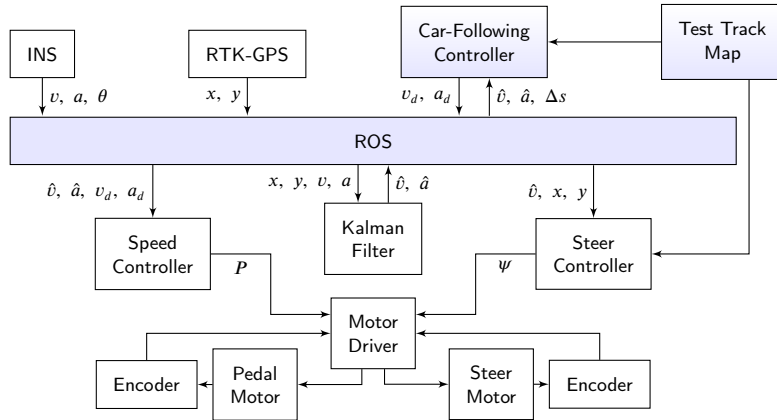


Figure 3: Structure of the low-level vehicle control system

5.1. Vehicle instrumentation

Testing consisted of one electric vehicle (Nissan Leaf) and one gasoline engine vehicle (Mazda CX-7). Both vehicles were not equipped with automated driving capabilities from the manufacturer, so they were modified to execute the commands from the high-level controller autonomously. The modifications include adding necessary sensors, actuators, and designing control algorithms.

5.1.1. Structure of low-level controller

The relationship between the sensors, actuators and controls in the low-level controller is shown in Figure 3. An inertial navigation system (INS) and RTK-GPS were added to each experimental vehicle. The INS measures vehicle speed v , acceleration a , and heading direction θ , while the RTK-GPS measures vehicle position (x, y) and publishes through ROS. A Kalman Filter (KF) fuses the speed, acceleration, and location information to obtain a more accurate estimate of the true vehicle speed \hat{v} and acceleration \hat{a} .

The low-level speed controller computes the desired position of the motor in the pedal actuator from the localization information, the estimate from the KF, and the desired speed v_d and acceleration a_d issued by the high-level car-following controller. The low-level steering controller takes input from a pre-configured waypoint map of the test track and computes the desired position of the motor in the steering wheel actuator from the localization information and the estimated speed. The motors in both the pedal actuator and the steering wheel actuator are driven by a two-channel motor driver. They both work under position control - and the position feedback is provided by high precision optical encoders.

5.1.2. Design of pedal and steering actuators

The pedal and steering wheel actuators were specially designed. They share a similar design for both vehicles, which is shown in Figure 4, despite minor adjustments made to accommodate different vehicle geometries. Both actuators are additionally powered with an emergency stop if intervention is required.

Figure 4 left shows the structure of the pedal actuator. The actuator was designed to only push either the accelerator or brake pedal, and so features a release mechanism which releases the engaged pedal before actuation switches to the

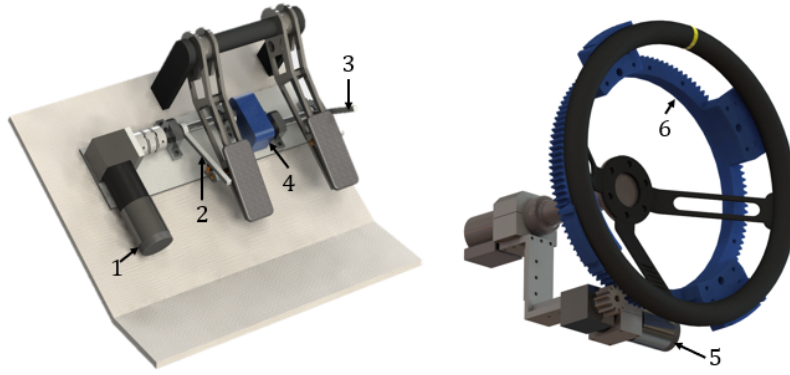


Figure 4: Specially designed actuators for pedal and steering wheel control

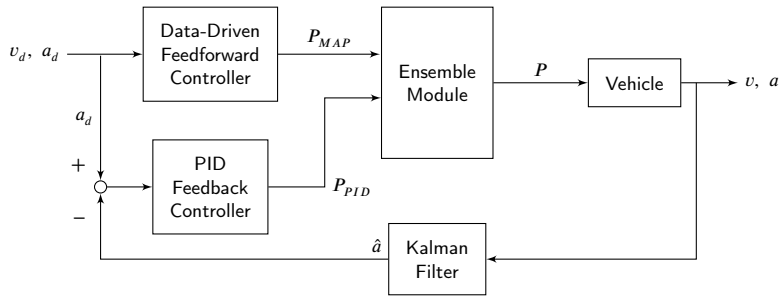


Figure 5: Pedal control system

other. This is accomplished through levers 2 and 3, which have different rotation directions: lever 2 is attached to the output shaft of electric motor 1, whereas lever 3 is attached to another shaft that is parallel to and connected to the motor shaft via gear drive 4. A lever can push down the corresponding pedal by applying force on a small cylinder that is protruding from the side of the pedal, but the lever itself is not rigidly fixed to the pedal. Thus when lever 2 rotates down, the brake pedal is pressed and the accelerator pedal is released - and vice versa.

Figure 4 right shows the structure of the steering wheel actuator. The electric motor 5 drives the gear ring 6 that is mounted behind the steering wheel so that the steering wheel can be rotated.

5.2. Low-level pedal controller design

Section 5.1 shows that longitudinal control of the vehicle is sought to be achieved by directly controlling the brake and accelerator pedals. However, the dynamics from pedals to vehicle motion is highly nonlinear due to the internal combustion engine, transmission (Li et al., 2010; McMahon et al., 1990), or batteries (Szumanowski and Chang, 2008; Bhangu et al., 2005). Moreover, the calibration map of the engine, transmission, or the battery was not available to us.

These factors make the implementation of solely a classical controller or solely a data-driven controller difficult here. Thus, the two approaches are fused to combine a data-driven feedforward controller with a classical PID feedback controller to solve the speed and acceleration tracking problem. The structure of the pedal controller is shown in Figure 5, which commands pedal position P given desired velocity v_d and acceleration a_d from the car-following control.

5.2.1. Data-driven feedforward control

With longitudinal control actuated through the pedals, we classify three different cases. Case 1 is control of the vehicle speed using the accelerator pedal - shown by the green area in Figure 6. This case is characterized by vehicle acceleration due to the accelerator pedal and deceleration due to coasting. Case 2 is high speed control of the vehicle deceleration using the brake pedal - shown by the red area in Figure 6. This occurs when vehicle deceleration needs to be achieved by the brake pedal. Case 3 occurs when attempting to control vehicle speed below idling, and is shown by the blue area in Figure 6.

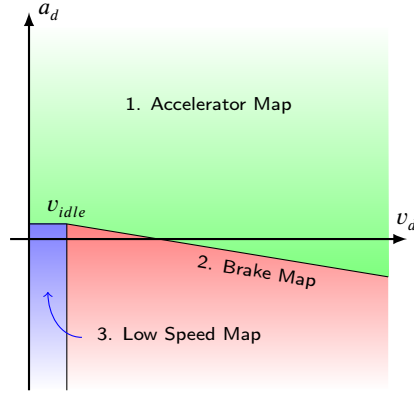


Figure 6: State space of the three different cases in longitudinal control

The candidate calibration map is required to map the target speed and acceleration to proper pedal position as accurately as possible. However, because the response of the vehicle is significantly different in each case, three separate maps (1. accelerator map, 2. brake map, and 3. low speed map) were identified and fitted. Thresholds between the maps are defined from coasting and idling data to determine the active region of the state space. Switching between maps was then introduced, with hysteresis bands included so that high-frequency toggling between modes does not occur.

The collection and classification of the calibration data for the maps was first done through calibration tests on a chassis dynamometer. Collecting data from such a controlled environment can help ensure minimum influence from environmental disturbances such as varying wind speed, road roughness, and grade. Data was gathered for the various configurations of accelerator and brake pedal positions to map the state space. When collecting data for the accelerator map, the vehicle was accelerated from standing to maximum speed through a range of accelerator positions. Likewise, data was collected for the brake map when decelerating the vehicle from maximum speed to standing through a range of brake positions. For the low speed map, the vehicle was brought to idle speed and then stopped through a range of brake positions.

In this paper, the three maps were fit with three-dimensional polynomial surfaces. They were calibrated from labeled data with vehicle speed and acceleration as input and pedal position P_{MAP} as target output. The order of the polynomial in each dimension was selected such that the surface fitting error is the minimum.

5.2.2. PID feedback control

While the three maps can describe the inverse vehicle response in a controlled environment, there remains inaccuracy in the calibration. Moreover, when the vehicle is driving on open roads, the air drag, road resistance, and grade will vary. An open-loop feedforward controller that only employs the calibration maps will not overcome these disturbances, particularly without a significant increase in the required calibration data. Thus, combining with a feedback controller can improve the low-level tracking performance. Here, a PID controller is introduced in feedback

$$P_{PID} = K_p e + K_i \int_0^t e dt + K_d \frac{de}{dt} \quad (11)$$

where $e = a_d - \hat{a}$ quantifies the tracking error from the car-following command a_d . The desired speed is then calculated open-loop by

$$v_d = v + a_d \Delta t \quad (12)$$

where Δt is the runtime of a control loop.

5.2.3. Fusion of data-driven feedforward and PID feedback controllers

The final pedal position output, P , is calculated by the ensemble module. In this paper, a complementary ensemble fuses the outputs of the data-driven feedforward and the PID controllers by

$$P = w P_{MAP} + (1 - w) P_{PID} \quad (13)$$

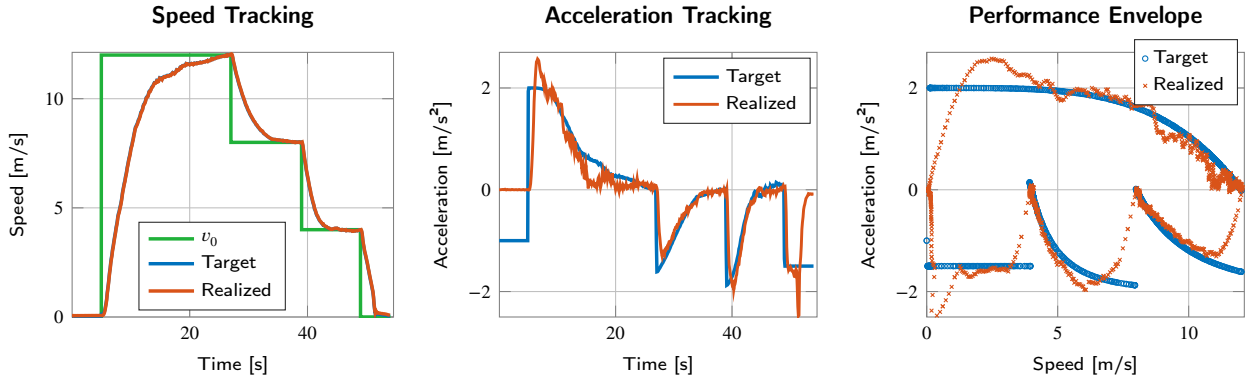


Figure 7: Mazda CX-7 speed profile tracking performance

where w is the weight coefficient of the fused controller. The weight coefficient w was tuned manually when driving on the test track so that the acceleration response of the vehicle did not show significant overshoot or overdamping.

5.3. Low-level steering controller design

A Pure Pursuit controller was implemented for the experimental vehicles to track the designated path of the test track. The steering input ψ to the vehicle is computed with the location of the target point l_d and the angle α between the vehicle's heading direction and the look-ahead direction

$$\psi = k \arctan\left(\frac{2L \sin \alpha}{l_d}\right) \quad (14)$$

where l_d is the look ahead distance given by

$$l_d = l_d^{min} + k_l v. \quad (15)$$

k_l and l_d^{min} are tunable gain and minimum look-ahead distance parameters. More complete details can be found in the literature, such as in (Amidi and Thorpe, 1991).

5.4. Low-level speed profile tracking performance

Both experimental vehicles were calibrated to follow a short square-wave speed profile while driving on a rough road with notable grade. A dynamic target generator was created based on the IDM from Eqn. (10), which calculates desired speed and desired acceleration from the speed profile.

$$a_d = a_0 \left(1 - \left(\frac{v}{v_0}\right)^\delta\right) \quad (16a)$$

$$v_d = v + a_d \Delta t \quad (16b)$$

Here, $a_0 = \pm 2.0 \text{ m/s}^2$ is the maximum acceleration, and v_0 is the target speed from the square-wave-shaped profile. The PID controllers of both vehicles were tuned to reject the road disturbance without notable overshoot.

The result is shown in Figure 7 and 8. The combined controller showed acceptable tracking response and achieved a steady state speed tracking error of $\pm 0.06 \text{ m/s}$ for both vehicles. The acceleration tracking was also accurate, where the performance envelope shows that the acceleration tracking was acceptable over the entire domain of velocity.

6. OBD-II energy measurement methods

An iOS app was created to pair with the On-Board Diagnostics (OBD-II) port of the vehicles with 29-bit ISO 15765-4 CAN protocol as in (Fayazi et al., 2019; Fayazi and Vahidi, 2017). The implemented iOS app connects to commercial WiFi OBD-II dongles supporting the ELM327 chip (ELM Electronics, 2012), as depicted in Figure 9.

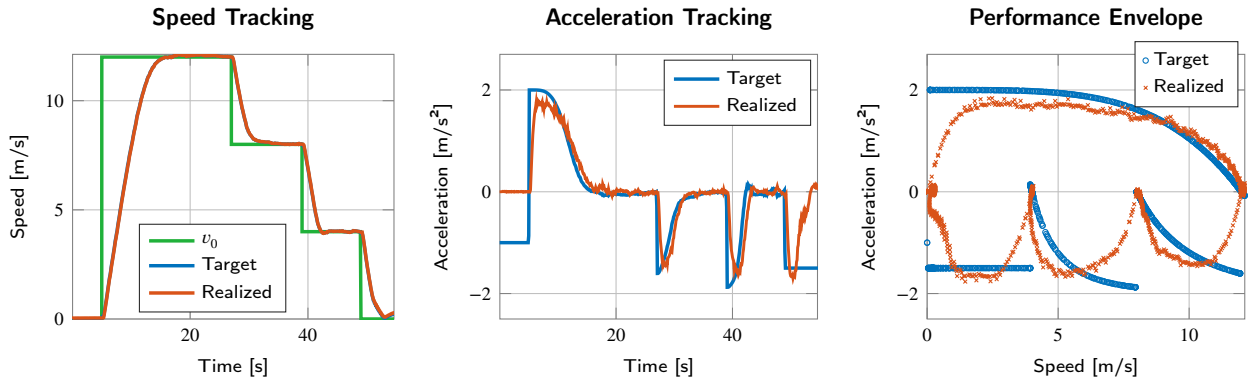


Figure 8: Nissan Leaf speed profile tracking performance



Figure 9: The AVL KMA Mobile fuel measurement system and the OBD-based fuel rate estimator connected to the combustion test vehicle

The app was extended to read the combustion engine Mazda CX7's 11-bit CAN protocol and the electric motor Nissan Leaf's unstandardized protocol. A custom procedure was programmed to increase the default data sampling frequency of the ELM chip. In total, data was collected from the Mazda at a rate of 8 hz, and data was collected from the Nissan at a rate of 4 hz. Finally, the app collected iOS GPS and timestamp data so that OBD-II readings could be correlated with simulation.

6.1. Internal combustion engine vehicle

First, fuel flow rate was modeled as a function of available OBD-II signals and one data-driven parameter. The fuel estimation model was then validated using fuel volume and flow data available from a flow meter during a chassis dynamometer calibration test. Finally, the calibrated model was applied to OBD-II data from the test track to record fuel consumption.

Figure 9 shows the flow meter calibration experiment, with an AVL KMA Mobile flow meter connected between the fuel tank and the high pressure fuel pump of the engine (Online, 2020a). The SoMat eDAQ system (Online, 2020c) was used with the SoMat Test Control Environment software to collect fuel data.

Fuel injector flow rate, pulse width, or a similar quantity was not available on the test vehicle, so fuel rate was modeled using ECU-estimated mass airflow (MAF), commanded λ , and a derived MAF correction curve. As background, the air-fuel ratio of a conventional gasoline engine is typically near stoichiometric to promote stable combustion, high efficiency, and low emissions. However, a mildly rich λ of 0.85 to 0.91 can increase maximum torque. Even richer mixtures are sometimes used to limit exhaust gas temperatures, particularly in turbocharged applications. The test vehicle's OBD-II data includes the ECU-commanded air-fuel ratio in the form of $\lambda = \dot{m}_{f_s} / \dot{m}_f$ where \dot{m}_{f_s} and \dot{m}_f denote the stoichiometric and actual mass fuel flow, respectively. The fuel flow that the ECU commands is modeled

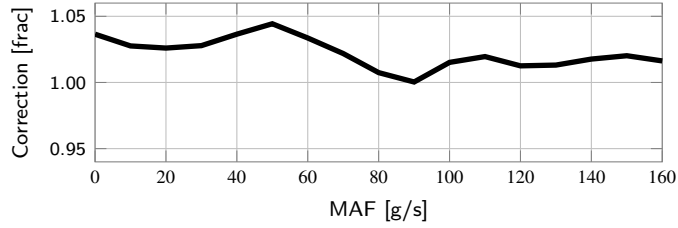


Figure 10: MAF correction factor and source fuel trim data

as follows.

$$\dot{m}_f = \frac{\dot{m}_a}{AFR_s \lambda_c} \bar{E}_A (\dot{m}_a) \quad (17)$$

A stoichiometric air-fuel ratio $AFR_s = 14.1$ was used for the 10% ethanol pump fuel that is commonly available in the United States.

In Eqn. (17), \bar{E}_A is a correction factor to the ECU-estimated mass airflow. λ is normally closed-loop controlled to stoichiometric using an exhaust oxygen sensor. Long-term and short-term correction factors called *trims* are applied to the fuel pulse width such that the desired λ is delivered. These trims are denoted *LTFT* and *STFT*, respectively. Errors in both airflow measurement and fuel system modeling contribute to these fuel trims. Assuming that fuel system model deviation results from a change in effective orifice size, Eqn. (18) assumes that the trim due to the fuel system is a constant e_F with respect to mass airflow.

$$E_A = 1 + \frac{LTFT + STFT}{100} - e_F \quad (18)$$

Transient gas exchange dynamics and measurement delays generally affect fuel trims and their time-alignment with airflow estimates. Fuel trims are therefore scattered as a function of airflow, although trends do emerge over large datasets. So, E_A is not used directly, but rather averaged into bins to calibrate \bar{E}_A - where M is the number of samples in the bin.

$$\bar{E}_A (\dot{m}_{aj}) = \frac{1}{M} \sum_{j=1}^M E_A \dot{m}_{aj} \quad (19)$$

6.1.1. Calibration and Validation

Closed-loop data from track tests of various algorithms was combined into a calibration dataset for \bar{E}_A . Figure 10 shows the resulting correction, which is within 5% for all \dot{m}_a .

The OBD-based fuel flow model was validated in two ways: dynamically by comparison against measurements from a volume flow meter, and cumulatively by comparison against a measured volume of fuel placed in the empty tank. This fuel was also weighed to ensure accurate density. Three tests were performed, all of which began with a certain amount of fuel in the tank. For each test, the vehicle was run on a chassis dynamometer until it ran out of fuel. Test 3, during which 3 US gallons of fuel was consumed, was used to calibrate e_F . Tests 1 and 2 were reserved for validation. Figure 11 demonstrates qualitative model performance in lower and higher power samples from Test 1.

Table 4 lists the model's accuracy in the three chassis dynamometer tests where total fuel volume was directly measured. Test 2's flow meter and volume-based cumulative fuel measurements differed by 8.0%, exceeding the differences observed in the other tests and indicating a possible ground truth measurement error in Test 2. Therefore, the proposed OBD-based technique was adopted by virtue of its close match to the validation data in test 1 and acceptable match to the instantaneous fuel flow measurement in Figure 11.

6.2. Battery electric vehicle

Unlike the combustion engine vehicle, the specification of the electric vehicle's OBD data is not published by the vehicle manufacturer - mainly because the electric car manufacturers have not established a standard for messages exchanged from its CAN bus (Tseng et al., 2016). The existing smart phone applications for Nissan Leaf's OBD data

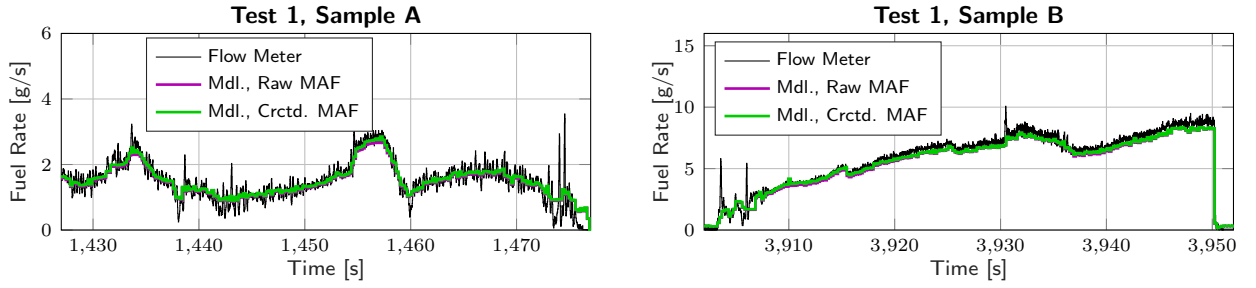


Figure 11: Comparison of OBD model-based fuel rate with and without MAF correction against fuel flow measurements

Table 4

OBD model accuracy in cumulative fuel consumption

Test No.	Meas. Fuel Vol. [L]	Est. Fuel Vol. [L]
1 (validation)	3.79	3.79
2 (validation)	9.46	8.90
3 (calibration)	11.36	11.38

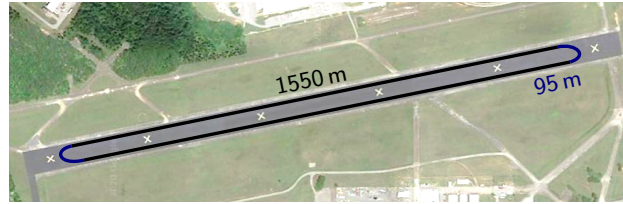


Figure 12: International Transportation Innovation Center (ITIC) testing grounds with virtual road markings and speed limit zones denoted. Black straight-aways had a speed limit of $\bar{v}_0 = 22.3$ m/s, while blue U-turns had a speed limit of $\bar{v}_1 = 7.0$ m/s. Base image retrieved from Google Maps

collection, such as Leaf Spy (Online, 2020b), provide insufficient sample rates. Following the guidelines in (Tseng et al., 2016) and verifying the results with that of Leaf Spy, OBD-based measurements were collected for the signed battery current, I , terminal voltage, V_T , state-of-charge, SOC , and capacity via the custom iOS app.

For the Li-ion battery of the Nissan Leaf, a lumped resistance R_s is considered. As shown in (Parvini et al., 2017), the open-circuit voltage, V_{OC} , is assumed to have a linear relationship with SOC in the mid-range of SOC levels when considering fixed battery temperature. So, the resulting linear model is fit to the collected OBD data to give an estimated value of $R_s = 0.1 \Omega$. As the obtained resistive loss is negligible compared to the battery net energy, and each test consisted of similar ambient temperatures, R_s was assumed constant for all tests. Considering the resistive energy loss, the battery net energy is then obtained by integrating over the entire test interval.

$$E_{battery} = \int_{t_0}^{t_1} [V_T(t) I(t) + R_s I^2(t)] dt \quad (20)$$

$$\approx \sum_{k=1}^M [V_T(t_{k-1}) I(t_{k-1}) + V_T(t_k) I(t_k) + R_s I^2(t_{k-1}) + R_s I^2(t_k)] \frac{\Delta t_k}{2} \quad (21)$$

7. Experimental scenario description

As mentioned in Section 2, the test track and simulation roads are mapped one-to-one by creating waypoints for the real and simulated vehicles to drive the same road network.

A picture of the testing grounds with the network overlay is given in Figure 12. Because the track was long and

narrow in geometry, it requires making U-turns to continue a simulation, and velocity is physically limited to a lower speed while making a U-turn. As such, control logic was defined for the high-level controllers to interact with the varied speed limits.

Three simulation variants of 1) a microsimulation environment, 2) the EPA US06, and 3) the EPA UDDS are taken to model traffic in the network, and are modified to match the test track requirements. 6 laps were run for the microsimulated experiments, and 3 laps were run for each of the drive cycle experiments.

7.1. Speed limit control logic

Recall particle kinematic equations of constant acceleration,

$$a_c ds = v dv \rightarrow \bar{v}_1^2 = \bar{v}_0^2 + 2a_c (s - s_0) \quad (22)$$

where $a_c = -2.0 \text{ m/s}^2$ is chosen as a comfortable deceleration to reach the U-turn velocity from straight-away velocity. The quantity $\delta s \triangleq s - s_0$ then describes the distance away from the U-turn speed limit \bar{v}_1 needed to slow down from straight-away speed limit \bar{v}_0 .

$$\delta s = \frac{\bar{v}_1^2 - \bar{v}_0^2}{2a_c} \quad (23)$$

For the WIE and IDM controllers, switching control can then be applied when within δs as

$$u^+ = \min \{u, a_c\} \quad (24)$$

where u is the control of the WIE or IDM continuous model, and u^+ is the control command to apply when approaching the U-turns. This logic limits the control to only engage in the most conservative acceleration that occurs due to either car-following or velocity maintenance.

For the MPC, Eqn. (3b) limits maximum velocity for each optimization stage. This poses challenges because the MPC optimization horizon is a function of time, whereas speed limit transitions are a function of distance instead.

An approximation is made to convert the velocity constraint to a function of time using an estimate of the ego's speed trajectory. In this case, a constant velocity is assumed in the speed estimate $\tilde{v}(i) = v$, $i = 0, \dots, N$. The position estimate then follows as $\tilde{s}(i+1) = \tilde{s}(i) + \tilde{v}(i)\Delta t_h$. Combining with Eqns. (22, 23), the following can then be used to define the MPC moving velocity constraint with s_l describing the current distance from the speed limit.

$$\bar{v}(i) = \begin{cases} \bar{v}_0 & \tilde{s}(i) < s_l \\ \sqrt{\bar{v}_0^2 + 2a_c (\delta s - (s_l - \tilde{s}(i)))} & \tilde{s}(i) < \delta s + s_l \\ \bar{v}_1 & \tilde{s}(i) \geq \delta s + s_l \end{cases} \quad (25)$$

Similar approaches can follow for the moving velocity constraint when approaching a higher velocity speed zone.

7.2. Microsimulator experiment

A PTV VISSIM microsimulation environment was set up which comprised of a single-lane circuit of 74 vehicles as depicted in Figure 1. The VISSIM human-driver model (as introduced in Section 4) controlled all simulated vehicles, with the exception of the MPC-C scenario, in which a string of 5 simulated CAVs plus the experimental CAV were controlled by the MPC. Because the vehicles start from rest, lap 1 is discarded to remove unwanted transient effects in simulation, and then the next 5 laps are considered for energy and traffic flow analysis. The scenario presented here can be physically motivated as a general car-following study consisting of a combination of on-ramps and off-ramps into highway driving, or a car-following study with forced slow-downs due to bottlenecks, etc.

As an improvement over some ring experiments, which can feature tight strings of vehicles which all interact together and thus form unrealistic disturbance propagation/attenuation, the experiments here use a larger road network with significant gap between the first and last vehicle in the string. This largely removed the ego vehicle's influence on traffic downstream. It was found the PV velocity profiles well-matched in behavior, as depicted in Figure 13, though some differences do exist due to bottle-necking that occurred at the U-turns.

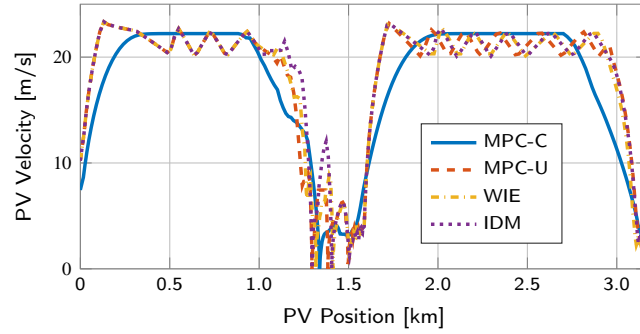


Figure 13: Microsimulation experimental velocity profiles of the PV for MPC-U, MPC-C, WIE, and IDM ego vehicle cases for lap 3

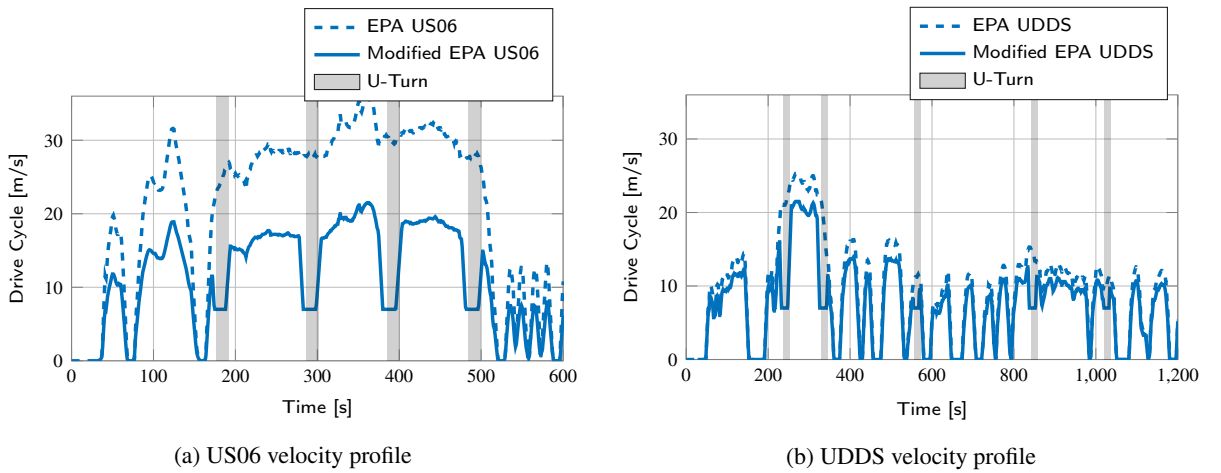


Figure 14: Modified EPA drive cycle experimental velocity profiles used for the PV

7.3. Modified EPA drive cycle experiments

Separate from the VISSIM microsimulation environment, a simulation environment consisting of a single preceding vehicle was created. The EPA US06 and EPA UDDS drive cycles were used to set the velocity profile of the PV ([United States Environmental Protection Agency \(EPA\), 2020](#)). These cycles target more specific acceleration-aggressive and urban-driving car-following scenarios and can serve as an upper-bound on energy benefits found with the MPC.

After setting an initial distance between the simulated PV and the physical ego vehicle of the car-following controller minimum distance \underline{d} , the real-time position of the PV at time t and the gap between the PV and ego vehicle are computed by interpolation. The drive cycles were looped until 3 laps were completed.

The velocity trajectories of US06 and UDDS cycles are scaled down by 40% and 20%, respectively, to match the speed limits at the test track. Due to speed limits at the U-turns, the drive cycles were also modified by the similar logic as given in Section 7.1 - the result of which is shown in Figure 14. For the MPC-C scenario, the PV's future position over the horizon \mathcal{S}_r is also communicated. While this is physically unrealistic with fixed drive cycles, a priori knowledge of the PV position provides an upper bound on the possible energy benefits the anticipative car-following MPC is capable of. Experimental results are given in Section 8.

8. VIL experimental results for energy efficiency and traffic flow

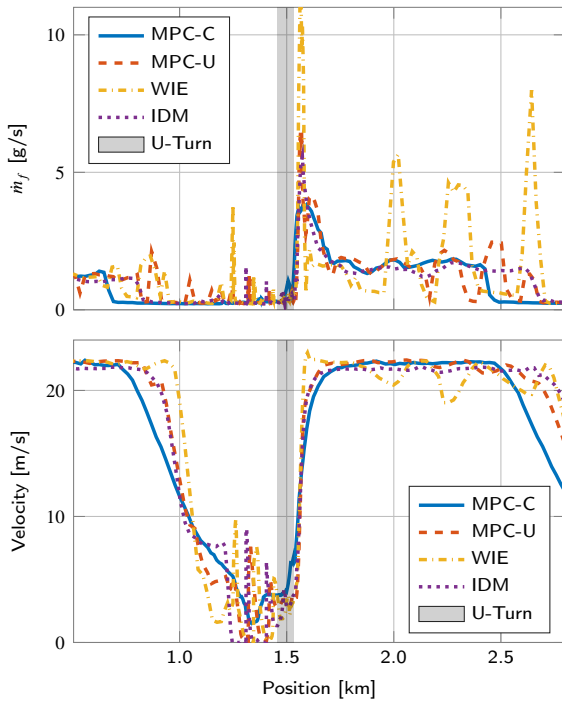
The results for the VIL experiments with the 3 simulation variants of microsimulator environment, EPA US06, and EPA UDDS are given for the ICEV Mazda CX7 and the EV Nissan Leaf. Here, all high-level controller types of Wiedemann 99 (WIE), Intelligent driver model (IDM), MPC unconnected (MPC-U), and MPC connected (MPC-C)

Table 5
 ICEV Mazda microsimulated controller performance

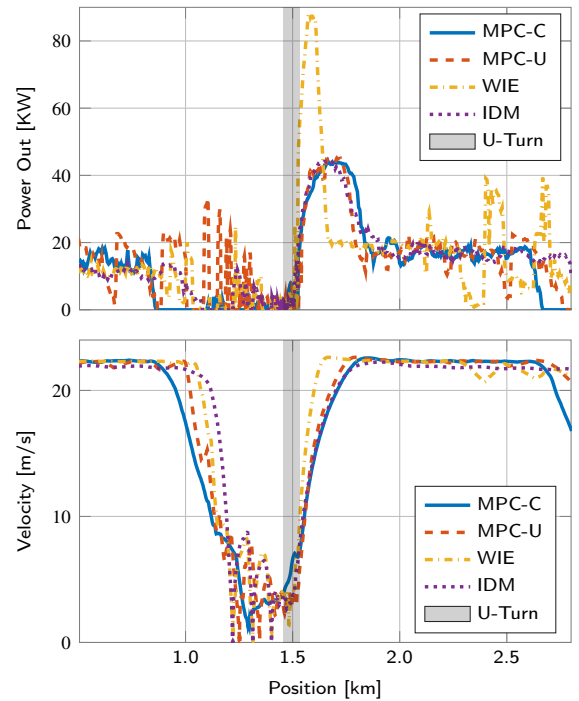
	WIE	IDM	MPC-U	MPC-C
Travel Time	24' 01"	23' 45" -1.1%	24' 00" 0%	23' 34" -1.9%
Avg. Headway [s]	3.47	5.73 +65.1%	3.32 -4.3%	2.75 -20.7%
Mean Gap [m]	28	59 +111%	37 +32%	28 0%
Max. Gap [m]	83	144 +73%	112 +35%	74 -11%
Net Fuel [L]	2.556	2.174 -15%	2.241 -12%	1.978 -23%

Table 6
 EV Nissan microsimulated controller performance

	WIE	IDM	MPC-U	MPC-C
Travel Time	23' 49"	23' 49" 0%	23' 40" -0.9%	23' 36" -1.9%
Avg. Headway [s]	3.96	5.81 +46.7%	2.93 -26.0%	2.82 -28.8%
Mean Gap [m]	27	62 +130%	31 +16%	32 +21%
Max. Gap [m]	76	151 +99%	96 +26%	82 +8%
Net Energy [kwh]	4.090	3.730 -8.8%	3.766 -7.9%	3.247 -20.6%



(a) ICEV microsimulated experiment



(b) EV microsimulated experiment

Figure 15: Experimental microsimulator comparison of the energy output rates (above) and the velocity profiles (below) for the high-level controllers for lap 3

were examined for both their energy and traffic flow impacts.

Realized headway for the ego vehicle was calculated as gap divided by ego velocity $T = \Delta s/v$, where data with a velocity below 0.1 m/s is discarded to avoid the singularity.

8.1. Microsimulated experimental results

The microsimulated experimental study gives better intuitions and general observations about the performance of the various controllers as compared to the drive cycle studies - largely because the driving patterns of the PV are clearly motivated by naturally emergent traffic stimuli. A summary of the microsimulated experiments is given in Tables 5 and 6 for the ICEV and EV, respectively.

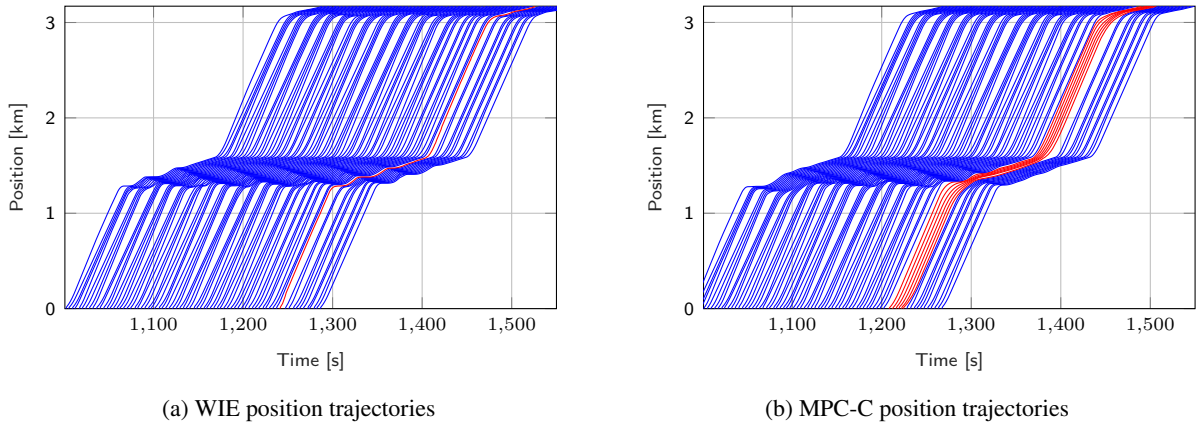


Figure 16: WIE and MPC-C ego (red) position trajectories over time against the virtual human traffic (blue) for lap 5 of the microsimulated experiment. The ego is the rearmost MPC vehicle in (b)

8.1.1. Energy Effects

The MPC offered energy efficiency improvements over the WIE driver for both the combustion engine and electric motor powertrains - as shown in Tables 5 and 6. In particular, MPC-U reduced energy usage by 12% and 8% for the ICEV and EV, respectively, whereas MPC-C reduced energy usage by 23% and 21% for the ICEV and EV, respectively. Additionally, it did not sacrifice realized time headway, and so the OCP defining the MPC was successful at balancing both eco-driving and traffic flow.

The speed limits impose additional disturbance in the network - apart from those arising due to natural longitudinal traffic patterns. While it is not feasible to quantify separate energy effects between the pure car-following behavior and the speed-maintenance behavior, Figure 15 indicates that the MPC improved the energy efficiency over the WIE in both cases. For the ICEV, WIE's higher fuel rate when accelerating out of the U-turns was caused not only by its higher engine output power, but also by enrichment at high power in this downsized-boosted engine. The four algorithms IDM, MPC-C, MPC-U, and WIE resulted in richest λ commands of 0.90, 0.88, 0.88, and 0.70, respectively - which reduced WIE's tank-to-wheels efficiency during acceleration maneuvers. The EV exhibited similar power consumption trends with the high-level controllers.

The IDM presented here additionally improved energy economies over the WIE, and even slightly out-performed the MPC-U for energy. However, as the IDM significantly increased its commanded gap and headway, it negatively impacted surrounding traffic flow in favor of reducing its own vehicle interactions.

Finally, Figure 16 depicts upstream traffic smoothing in the MPC-C case as compared to the baseline WIE case. To this end, the traffic was assumed to be composed of mid-sized combustion vehicles, and energy impact of the virtual upstream traffic smoothing was estimated using the fuel model developed in (Dollar and Vahidi, 2018). Comparing the fuel usage of the upstream traffic for each high level controller to the WIE case, it was found that the MPC-C scenario improved fuel usage of upstream traffic by 4.5% on average, the MPC-U scenario improved fuel usage of upstream traffic by 0.4% on average, and the IDM *worsened* their fuel usage by 0.9%. By this, automated vehicles and connectivity have the potential to provide secondary benefits for improving the energy usage of neighboring traffic.

8.1.2. Traffic flow effects

The traffic flow behavior in simulation can then be further studied. It can be observed that both MPC cases reduced average time headway as compared to the baseline WIE model. This supports that the MPC can improve traffic flow over human-like drivers, and was accomplished despite less aggressive driving out of the U-turns - which lead to increases in gap.

Figure 16 depicts the position trajectories of each vehicle over time. Platoons can be clearly observed as strings of vehicles begin to compact at high velocity, and velocities decrease around the mid and endpoints of the track due to speed limit interactions with the U-turns. One can then observe stop-and-go behavior by the ripples in the position trajectories, which is detrimental to the energy economy of the fleet of vehicles.

Differences in the behavior of the 11 vehicles upstream of the ego highlight the smoothing effects of the CAVs

Table 7
ICEV Mazda US06 controller performance

	WIE	IDM	MPC-U	MPC-C
Travel Time	9' 20"	9' 33" +2.3%	9' 20" 0%	9' 26" +1.1%
Avg. Headway [s]	2.45	6.23 +154.3%	2.64 +7.8%	2.66 +8.6%
Avg. Gap [m]	23	35 +52%	26 +13%	23 0%
Max. Gap [m]	40	93 +133%	77 +93%	88 +120%
Net Fuel [L]	1.006	0.840 -17%	0.746 -26%	0.684 -32%

Table 8
EV Nissan US06 controller performance²

	WIE	IDM	MPC-U	MPC-C
Travel Time	8' 39"	8' 39" 0%	8' 38" 0%	8' 39" 0%
Avg. Headway [s]	2.14	5.80 +171.0%	2.76 +29.0%	2.58 +20.6%
Avg. Gap [m]	24	38 +58%	28 +17%	25 +4%
Max. Gap [m]	42	92 +119%	78 +86%	82 +95%
Net Energy [kwh]	1.286	1.230 -4%	1.064 -17%	0.963 -25%

on the fleet: as opposed to the WIE scenario, the CAV string attenuated disturbances of the traffic and subsequently smoothed the driving of the vehicles behind. The MPC-C scenario smoothed traffic the most, and it was found the MPC-U scenario smoothed traffic some - even with only a single automated vehicle present. IDM did not visually affect upstream traffic upon inspection. The energy impact from this traffic attenuation is discussed in Section 8.1.1.

The position trajectories of the first several vehicles in the string differs between the WIE and MPC-C cases. As discussed in Section 7, however, this occurred due to bottle-necking at the U-turns, and largely did not influence the ego vehicle results.

The IDM used here was, in short, unacceptable for traffic flow because of its large spacing and headway commanded - increasing them by 130% and 65%, respectively. Despite this, IDM was still able to command acceptable travel times because it was able to maintain high velocity for longer periods of time. This largely negates the energy benefits for IDM as seen in Tables 5 and 6.

8.2. Modified US06 drive cycle results

As shown in Tables 7 and 8, the MPC energy economy was significantly improved over the WIE model - with the modest increase in average headway. Overall, the MPC improved the combustion vehicle energy performance by 26% and 32% for the unconnected and connected variants, while the MPC improved the electric vehicle energy performance by 17% and 25% for the unconnected and connected variants. Additionally, Figure 17a gives the fuel rate and velocity trajectories of each of the ICEV controllers for a portion of the first lap of the US06. Figure 18a gives the battery output/input power and velocity trajectories of each of the EV controllers for a portion of the first lap of the US06.

In contrast to the microsimulated experiment, it was observed that the MPC cases had worse time headway as compared to the baseline WIE model when simulating the US06. Similar to some humans, the WIE model can violate the speed limit in favor of catching the front vehicle, whereas MPC is soft-constrained to avoid speeding. This can improve the WIE model's headway tracking when considering highly acceleration-aggressive PV cycles such as the US06. In addition, the MPC was heavily penalized against acceleration, which then trades off its ability to track the PV during high acceleration periods. In short, the MPC parameters worked well for the microsimulated experiment, but could be improved for the US06 scenario - and so the MPC performance may benefit from adaptive tunings. This result is interesting and could motivate further studies.

As before, the IDM exhibited poor headway performance. The IDM is constrained with an upper-bound on acceleration capabilities instead of a velocity-dependent acceleration constraint like the MPC and WIE model, which can be too conservative in low-velocity driving and particularly ineffective in scenarios such as this one with large accelerations exhibited by the PV.

8.3. Modified UDDS drive cycle results

A summary of the modified UDDS experiments is given in Tables 9 and 10 for the ICEV and EV, respectively. Here, the MPC significantly improved energy economy over the baseline human-like driver. The MPC improved the combustion vehicle energy performance by 14% and 24% for the unconnected and connected variants, while the MPC improved the electric vehicle energy performance by 25% and 34% for the unconnected and connected variants.

²EV Nissan modified US06 results were shortened to the first 520s due to loss of some OBD-II data.

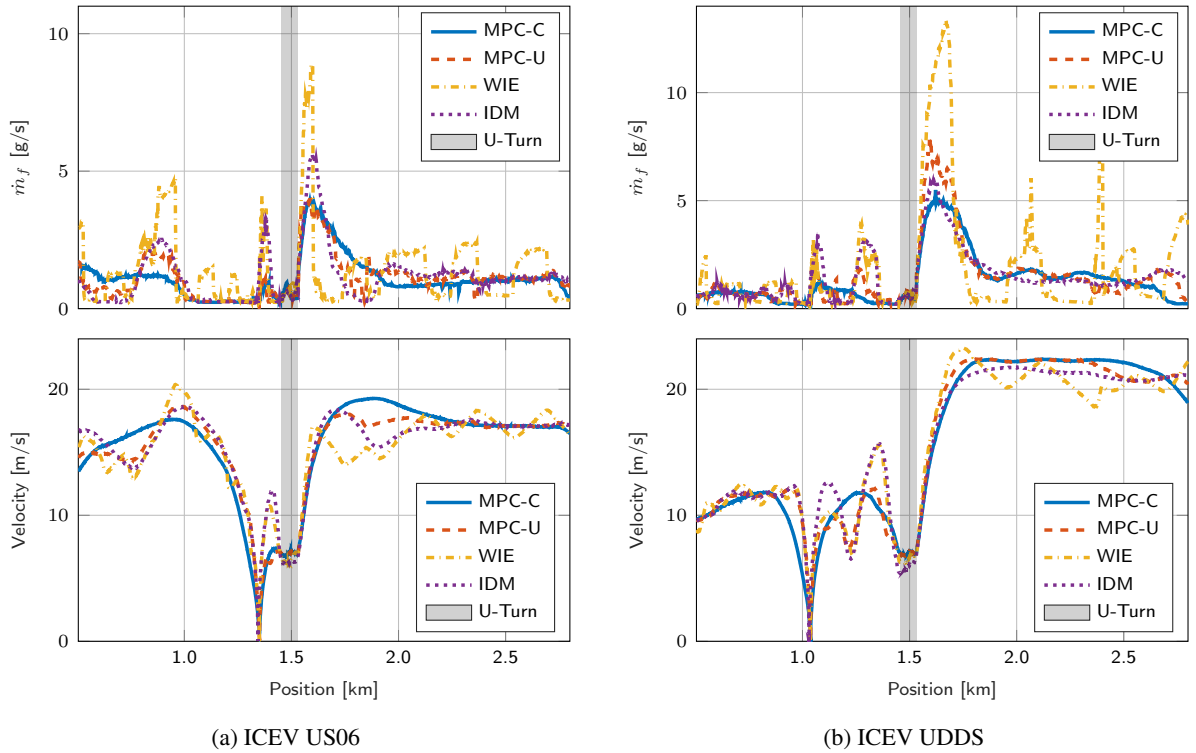


Figure 17: Drive cycle comparison of the ICEV fuel rates (above) and the velocity profiles (below) for the high-level controllers for lap 1

Table 9
ICEV Mazda UDSS controller performance

	WIE	IDM	MPC-U	MPC-C
Travel Time	22' 33"	22' 36" +0.2%	22' 35" +0.1%	22' 36" +0.2%
Avg. Headway [s]	3.39	5.94 +75.2%	2.85 -15.9%	3.53 +4.1%
Avg. Gap [m]	16	22 +38%	16 0%	20 +25%
Max. Gap [m]	46	99 +115%	83 +80%	70 +52%
Net Fuel [L]	1.370	1.329 -3%	1.175 -14%	1.048 -24%

Table 10
EV Nissan UDSS controller performance

	WIE	IDM	MPC-U	MPC-C
Travel Time	22' 33"	22' 35" +0.1%	22' 34" +0.1%	22' 34" +0.1%
Avg. Headway [s]	4.22	4.39 +4.0%	2.51 -40.5%	3.15 -25.4%
Avg. Gap [m]	16	22 +38%	15 -6%	19 +19%
Max. Gap [m]	43	111 +158%	85 +98%	79 +84%
Net Energy [kwh]	1.855	1.639 -12%	1.389 -25%	1.221 -34%

Additionally, Figure 17b gives the fuel rate and velocity trajectories of each of the ICEV controllers for a portion of the first lap of the UDSS. Figure 18b gives the battery output/input power and velocity trajectories of each of the EV controllers for a portion of the first lap of the UDSS.

Both MPC improved average headway like shown in the microsimulated experiment. Though, of note, the UDSS cycle emerged distinct behavior for the MPC when using connectivity: the MPC-C controller exhibited a noticeably larger average headway than the MPC-U case. The connected case is typically intended to drive closer to the PV to improve traffic compactness but, because it has full preview of the UDSS for its prediction horizon, it sacrifices following distance in favor of improved acceleration minimization. This understanding can be motivated by the frequent stopping of the UDSS, where future stops are in preview, and so the MPC-C cuts wasteful acceleration and subsequent braking.

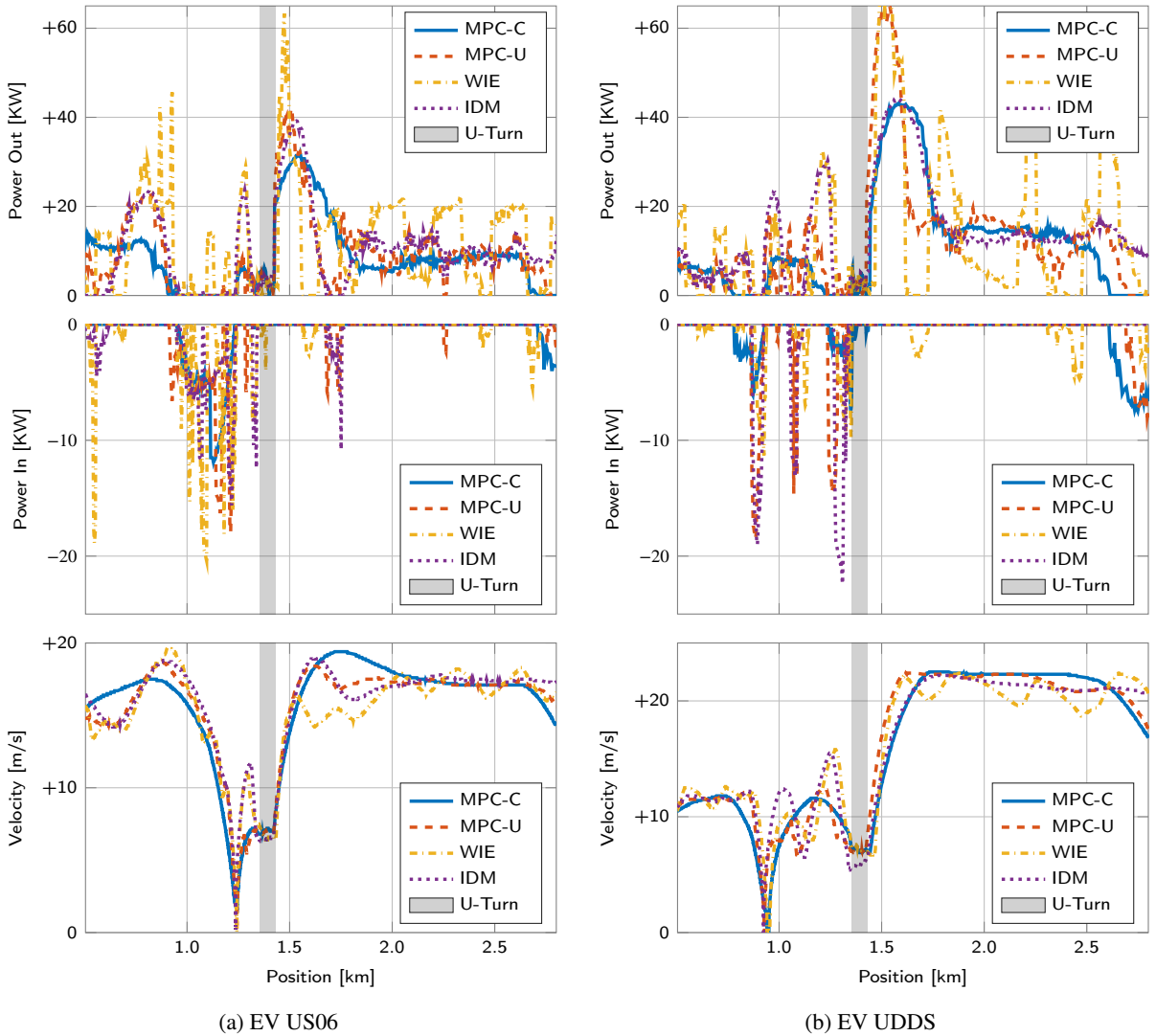


Figure 18: Drive cycle comparison of the EV battery power (above), regenerative power (middle), and the velocity profiles (below) for the high-level controllers for lap 1

9. Conclusion

Experiments were conducted on both a combustion engine vehicle and electric motor vehicle to evaluate their energy and traffic performance using chance-constrained model predictive control for vehicle guidance. Both vehicles were equipped for autonomy by fitting pedal and steering actuators to control their acceleration and pose. In particular, a novel data-driven approach to vehicle pedal control was executed, and fused classical methods with a feedforward map to approximate the powertrain nonlinearities.

A Vehicle-in-the-Loop environment was designed to embed a physical vehicle into virtual reality with simulated traffic. Three separate experimental scenarios were designated to cover a variety of traffic conditions: a microsimulation experiment was conducted to study emergent highway-conditioned car-following, the US06 was simulated for the preceding vehicle to stimulate aggressive acceleration, and the UDDS was simulated for the preceding vehicle to create urban conditions.

The MPC is designed to minimize commanded acceleration and error in headway tracking for each CAV. When following another MPC vehicle it leverages connectivity to better plan control decisions, and in the absence of connectivity it quantifies uncertainty in prediction of the front human driver to balance safety with traffic compactness.

It was found the MPC outperformed the human-like driver models with regards to both realized headway and energy economy. Overall, the microsimulation experiment showed the MPC improved energy efficiency by 12% and 8% for the combustion and electric vehicles when following human drivers. Benefits were even greater in the drive cycle studies, where the US06 showed 26% and 17% improved energy efficiency for the combustion and electric vehicles, whereas the UDDS showed 14% and 25% improved energy efficiency for the combustion and electric vehicles.

Finally, once introducing connectivity, between 6-12% additional improvement in energy efficiency was found for the MPC compared with its unconnected variant. We also estimated secondary impacts of connectivity on traffic upstream of the ego vehicle, and found that 4.5% energy benefit was achieved for the 11 following drivers on average.

A. Protocol buffer structure

The data exchanged between the physical vehicles and simulation server lies in four categories with their data structure shown in Figure 19. Each message is preceded with a predefined preamble after being serialized by Google Protocol Buffers (Google Inc., 2020). In order to reduce the bandwidth challenges imposed on the simulation side, we incorporate the vehicle-to-vehicle (V2V) messaging into the Sim2V and V2Sim messages. The resulting buffer is only a few hundred bytes in size.

B. Wiedemann 99 model

The Wiedemann 99 model expands on the model proposed in (Wiedemann, 1974) for use in modeling human drivers.

Figure 20 gives the Wiedemann 99 model used in the experiments. The family of sd variables pertain to following and speed thresholds for the various logic in the model, $\mathcal{X} \in [0, 1]$ is a random variable unique to the driver with expected value 0.5, \mathcal{V} and \mathcal{A} are variables of speed difference perception and max acceleration aggressiveness, CC_j are the tunable Wiedemann 99 parameters, v is the ego velocity, v_r is the PV velocity, $\Delta v \triangleq v_r - v$ is the difference in velocities from the PV, \bar{v} is the max velocity, Δs is the gap from the PV, a_i is the current acceleration of the ego, a_{i+1} is the acceleration command of the ego, and a_r is the acceleration of the PV. Additionally, FS is the following state of the ego: it is assigned to a string describing the current action of the ego, where ‘A’ is increase distance, ‘B’ is decrease distance, ‘f’ is keep distance, ‘w’ is keep speed (Vortisch, 2020).

Acknowledgment

This work was supported by an award from the U.S. Department of Energy Vehicle Technologies Office (Project DE-EE0008469). The authors would like to thank Dr. Joachim Taiber and the International Transportation Innovation Center (ITIC) for reduced-fee access to the testing grounds throughout the project. They also thank Mr. Dominik Karbowski for contributing to discussion, thank Mr. David Mann for his technical support in dynamometer testing, and thank Professor Zoran Filipi for access to the International Center for Automotive Research (ICAR) facilities.

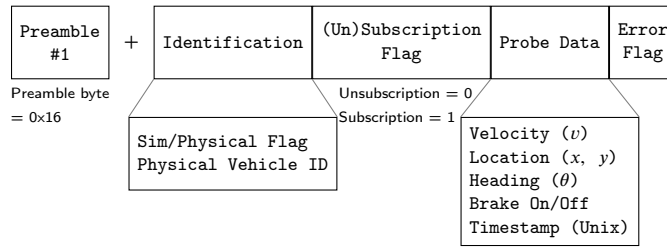
CRedit authorship contribution statement

Tyler Ard: Methodology, Software, Validation, Formal Analysis, Investigation, Data Curation, Writing - original draft. **Longxiang Guo:** Methodology, Software, Investigation, Writing - Review & Editing. **Robert Austin Dollar:** Methodology, Data Curation, Formal Analysis, Writing - Review & Editing. **Alireza Fayazi:** Software, Data Curation, Validation, Formal Analysis, Writing - Review & Editing, Supervision. **Nathan Goulet:** Investigation, Writing - Review & Editing. **Yunyi Jia:** Conceptualization, Supervision, Funding Acquisition, Writing - Review & Editing. **Beshah Ayalew:** Conceptualization, Supervision, Funding Acquisition, Writing - Review & Editing. **Ardalan Vahidi:** Conceptualization, Supervision, Project Administration, Funding Acquisition, Writing - review & editing.

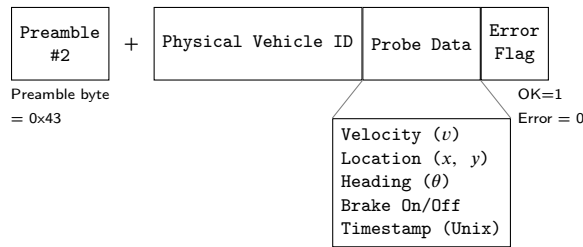
References

- Alexander, G., Lunenfeld, H., 1986. Driver expectancy in highway design and traffic operations. U.S. Department of Transportation Federal Highway Administration .
- Amidi, O., Thorpe, C.E., 1991. Integrated mobile robot control. *Mobile Robots V* 1388, 504–523. doi:10.1117/12.25494.

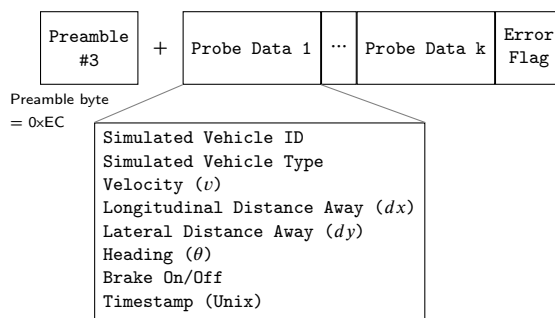
Subscription/Unsubscription Message:



V2Sim Message:



Sim2V Message:



V2V Message:

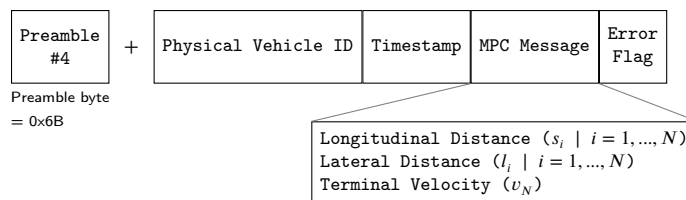


Figure 19: Four different message types implemented for the VIL test environment (Protocol buffer structured messages preceded with a preamble)

Ard, T., Ashtiani, F., Vahidi, A., Borhan, H., 2020. Optimizing gap tracking subject to dynamic losses via connected and anticipative MPC in truck platooning. Proceedings of the American Control Conference .

Ard, T., Dollar, R.A., Vahidi, A., Zhang, Y., Karbowski, D., 2019. Microsimulation of energy and flow effects from optimal automated driving in mixed traffic. arXiv preprint arXiv:1911.06818 .

Bhangu, B.S., Bentley, P., Stone, D.A., Bingham, C.M., 2005. Nonlinear observers for predicting state-of-charge and state-of-health of lead-acid batteries for hybrid-electric vehicles. IEEE transactions on vehicular technology 54, 783–794.

Chen, X., Li, L., Zhang, Y., 2010. A markov model for headway/spacing distribution of road traffic. IEEE Transactions on Intelligent Transportation

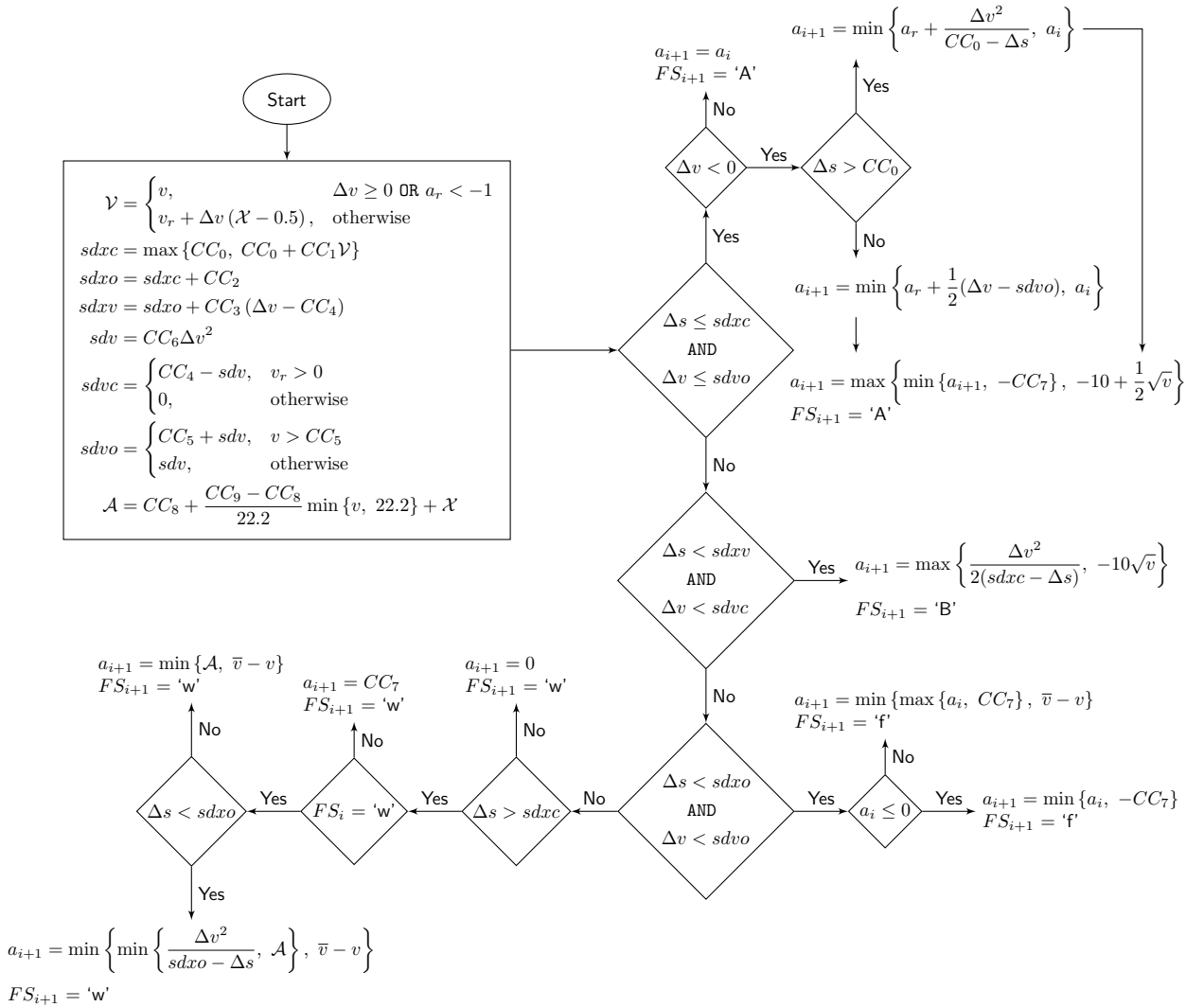


Figure 20: Algorithm of the Wiedemann 99 model used

Systems 11, 773–785. doi:10.1109/TITS.2010.2050141.

Dollar, R.A., Vahidi, A., 2018. Efficient and collision-free anticipative cruise control in randomly mixed strings. *IEEE Transactions on Intelligent Vehicles* 3, 439–452.

Dollar, R.A., Vahidi, A., 2019. Automated vehicles in hazardous merging traffic: A chance-constrained approach. *IFAC-PapersOnLine* 52, 218–223.

ELM Electronics, 2012. ELM327, OBD to RS232 interpreter. URL: <https://www.elmelectronics.com/wp-content/uploads/2017/01/ELM327DS.pdf>.

Fayazi, S.A., Vahidi, A., 2017. Vehicle-in-the-loop (VIL) verification of a smart city intersection control scheme for autonomous vehicles, in: 2017 IEEE Conference on Control Technology and Applications (CTA), IEEE. pp. 1575–1580.

Fayazi, S.A., Vahidi, A., Luckow, A., 2019. A vehicle-in-the-loop (VIL) verification of an all-autonomous intersection control scheme. *Transportation Research Part C: Emerging Technologies* 107, 193 – 210. URL: <http://www.sciencedirect.com/science/article/pii/S0968090X19310745>, doi:<https://doi.org/10.1016/j.trc.2019.07.027>.

Fellendorf, M., Vortisch, P., 2011. Microscopic traffic flow simulator VISSIM. *Fundamentals of Traffic Simulation*. International Series in Operations Research and Management Science, 63–93doi:10.1007/978-1-4419-6142-6_2.

Gao, Y., Gray, A., Carvalho, A., Tseng, H.E., Borrelli, F., 2014. Robust nonlinear predictive control for semiautonomous ground vehicles, in: 2014 American Control Conference, pp. 4913–4918.

Google Inc., 2020. Protocol buffers. URL: <https://developers.google.com/protocol-buffers>.

Gunter, G., Gloudemans, D., Stern, R.E., McQuade, S., Bhadani, R., Bunting, M., Monache, M.L.D., Lysecky, R., Seibold, B., Sprinkle, J., Piccoli, B., Work, D.B., 2019. Are commercially implemented adaptive cruise control systems string stable? 19122, 1–22. URL: <http://>

//arxiv.org/abs/1905.02108, arXiv:1905.02108.

- Gurobi Optimization, 2020. Gurobi optimizer reference manual. URL: <https://www.gurobi.com/documentation/>.
- Hajdu, D., Ge, J.I., Insuperger, T., Orosz, G., 2020. Robust design of connected cruise control among human-driven vehicles. *IEEE Transactions on Intelligent Transportation Systems* 21, 749–761.
- Han, J., Vahidi, A., Sciarretta, A., 2019. Fundamentals of energy efficient driving for combustion engine and electric vehicles: An optimal control perspective. *Automatica* 103, 558–572.
- Kamal, M.A., Mukai, M., Murata, J., Kawabe, T., 2011. Ecological driving based on preceding vehicle prediction using MPC. *IFAC Proceedings Volumes (IFAC-PapersOnline)* 44, 3843–3848. URL: <http://dx.doi.org/10.3182/20110828-6-IT-1002.02748>, doi:10.3182/20110828-6-IT-1002.02748.
- Li, S., Li, K., Rajamani, R., Wang, J., 2010. Model predictive multi-objective vehicular adaptive cruise control. *IEEE Transactions on Control Systems Technology* 19, 556–566.
- Liu, H., Shladover, S.E., Lu, X.Y., Kan, X., 2020. Freeway vehicle fuel efficiency improvement via cooperative adaptive cruise control. *Journal of Intelligent Transportation Systems: Technology, Planning, and Operations* 0, 1–13. doi:10.1080/15472450.2020.1720673.
- McMahon, D.H., Hedrick, J.K., Shladover, S.E., 1990. Vehicle modelling and control for automated highway systems, in: 1990 American Control Conference, IEEE. pp. 297–303.
- Mills, D.L., 2010. *Computer Network Time Synchronization: The Network Time Protocol on Earth and in Space*, Second Edition. 2nd ed., CRC Press, Inc., USA.
- NTSB Media Relations, 2020. Tesla crash investigation yields 9 NTSB safety recommendations. URL: <https://www.ntsbt.gov/news/press-releases/Pages/NR20200225.aspx>.
- Online, 2020a. AVL KMA mobile fuel consumption measurement system. URL: <https://www.avl.com/web/guest/-/avl-kma-mobile>.
- Online, 2020b. Leafspy pro. URL: <https://apps.apple.com/us/app/leafspy-pro/id967376861>.
- Online, 2020c. Somat eDAQ and Somat eDAQXR data acquisition systems. URL: <https://www.hbm.com/en/7775/edaqxr-edaq-mobile-rugged-data-acquisition-systems/>.
- Parvini, Y., Vahidi, A., Fayazi, S.A., 2017. Heuristic versus optimal charging of supercapacitors, lithium-ion, and lead-acid batteries: An efficiency point of view. *IEEE Transactions on Control Systems Technology* 26, 167–180.
- Ploeg, J., Scheepers, B.T., Van Nunen, E., Van De Wouw, N., Nijmeijer, H., 2011. Design and experimental evaluation of cooperative adaptive cruise control. *IEEE Conference on Intelligent Transportation Systems, Proceedings, ITSC*, 260–265doi:10.1109/ITSC.2011.6082981.
- Pomerleau, D.A., 1990. *Alvinn, an autonomous land vehicle in a neural network* URL: https://kithub.cmu.edu/articles/ALVINN_an_autonomous_land_vehicle_in_a_neural_network/6603146, doi:10.1184/R1/6603146.v1.
- Pourabdollah, M., Björkvik, E., Furer, F., Lindenberg, B., Burgdorf, K., 2017. Calibration and evaluation of car following models using real-world driving data, in: 2017 IEEE 20th International Conference on Intelligent Transportation Systems (ITSC), pp. 1–6.
- Rios-Torres, J., Malikopoulos, A.A., 2017. Automated and cooperative vehicle merging at highway on-ramps. *IEEE Transactions on Intelligent Transportation Systems* 18, 780–789. doi:10.1109/TITS.2016.2587582.
- Rios-Torres, J., Malikopoulos, A.A., 2018. Impact of partial penetrations of connected and automated vehicles on fuel consumption and traffic flow. *IEEE Transactions on Intelligent Vehicles* 3, 453–462. doi:10.1109/TIV.2018.2873899.
- Schmied, R., Waschl, H., Quirynen, R., Diehl, M., Del Re, L., 2015. Nonlinear MPC for emission efficient cooperative adaptive cruise control. *IFAC-PapersOnline* 48, 160–165. URL: <http://dx.doi.org/10.1016/j.ifacol.2015.11.277>, doi:10.1016/j.ifacol.2015.11.277.
- Stern, R.E., Cui, S., Delle Monache, M.L., Bhadani, R., Bunting, M., Churchill, M., Hamilton, N., Haulcy, R., Pohlmann, H., Wu, F., Piccoli, B., Seibold, B., Sprinkle, J., Work, D.B., 2018. Dissipation of stop-and-go waves via control of autonomous vehicles: Field experiments. *Transportation Research Part C: Emerging Technologies* 89, 205–221. URL: <https://doi.org/10.1016/j.trc.2018.02.005>, doi:10.1016/j.trc.2018.02.005, arXiv:1705.01693.
- Szumanowski, A., Chang, Y., 2008. Battery management system based on battery nonlinear dynamics modeling. *IEEE transactions on vehicular technology* 57, 1425–1432.
- Talebpour, A., Mahmassani, H.S., 2016. Influence of connected and autonomous vehicles on traffic flow stability and throughput. *Transportation Research Part C: Emerging Technologies* 71, 143–163. URL: <http://dx.doi.org/10.1016/j.trc.2016.07.007>, doi:10.1016/j.trc.2016.07.007.
- Thrun, S., et al., 2006. Stanley: The robot that won the DARPA grand challenge. *Journal of Field Robotics* 23, 661–692. doi:10.1002/rob.20147.
- Treiber, M., Hennecke, A., Helbing, D., 2000. Congested traffic states in empirical observations and microscopic simulations. *Physical review E* 62, 1805.
- Tseng, C.M., Zhou, W., Al Hashmi, M., Chau, C.K., Song, S.G., Wilhelm, E., 2016. Data extraction from electric vehicles through OBD and application of carbon footprint evaluation, in: *Proceedings of the Workshop on Electric Vehicle Systems, Data, and Applications*, pp. 1–6.
- Turri, V., Kim, Y., Guanetti, J., Johansson, K.H., Borrelli, F., 2017. A model predictive controller for non-cooperative eco-platooning. *Proceedings of the American Control Conference*, 2309–2314doi:10.23919/ACC.2017.7963297.
- United States Environmental Protection Agency (EPA), 2020. Dynamometer drive schedules. URL: <https://www.epa.gov/vehicle-and-fuel-emissions-testing/dynamometer-drive-schedules>.
- Vahidi, A., Sciarretta, A., 2018. Energy saving potentials of connected and automated vehicles. *Transportation Research Part C: Emerging Technologies* 95, 822–843.
- Vortisch, P., 2020. Where I can find the mathematical formulation of Wiedemann 99 car following model? URL: https://www.researchgate.net/post/Where_I_can_find_the_mathematical_formulation_of_Wiedemann_99_car_following_model.
- Wan, N., Zhang, C., Vahidi, A., 2017. Probabilistic anticipation and control in autonomous car following. *IEEE Transactions on Control Systems Technology* 27, 30–38.
- Washington State Department of Transportation (WSDOT), 2014. Protocol for VISSIM simulation. URL: <http://www.oregon.gov/ODOT/TD/TP/APM/AddC.pdf>.

- Wiedemann, R., 1974. Simulation des strassenverkehrsflusses, Institut für Verkehrswesen der Universität Karlsruhe.
- Woody, T., 2006. Calibrating freeway simulation models in VISSIM. Technical Report. University of Washington. Seattle, WA.
- Zhang, C., Vahidi, A., 2011. Predictive cruise control with probabilistic constraints for eco driving. ASME 2011 Dynamic Systems and Control Conference and Bath/ASME Symposium on Fluid Power and Motion Control, DSCC 2011 2, 233–238. doi:10.1115/DSCC2011-5982.
- Zheng, Y., Li, S.E., Li, K., Borrelli, F., Hedrick, J.K., 2017. Distributed model predictive control for heterogeneous vehicle platoons under unidirectional topologies. IEEE 25, 899–910. doi:10.1109/TCST.2016.2594588.